

EVOLUTION IN THE COLOR–MAGNITUDE RELATION OF EARLY–TYPE GALAXIES IN CLUSTERS OF GALAXIES AT $Z \sim 1$ ¹

B. P. HOLDEN^{2,3}, S. A. STANFORD^{2,4}
Department of Physics, University of California, Davis

P. EISENHARDT⁴
Jet Propulsion Laboratory, California Institute of Technology, MS 169-327, 4800 Oak Grove Drive, Pasadena, CA 91109

AND

M. DICKINSON⁴
Space Telescope Science Institute⁵, 3700 San Martin Dr., Baltimore, Maryland 21218
Draft version July 27, 2021

ABSTRACT

We present a study of the color evolution of elliptical and S0 galaxies in six clusters of galaxies inside the redshift range $0.78 < z < 1.27$. For each cluster, we used imaging from the Hubble Space Telescope to determine morphological types of the galaxies. These types were determined both by an automated technique and from visual inspection. We performed simulations to determine the accuracy of the automated classifications and found a success rate of $\sim 75\%$ at $m(L_*)$ or brighter magnitudes for most of our HST imaging data with the fraction of late–type galaxies identified as early–type galaxies to be $\sim 10\%$ at $m(L_*)$ to $\sim 20\%$ at $m(L_* + 2)$. From ground based optical and near-infrared imaging, we measured the zero-point and scatter in the color–magnitude relation of the elliptical and S0 galaxy populations, which we combine with the previous sample of Stanford et al. (1998), yielding a sample of cluster early–type galaxies that span a lookback time of almost 9 gigayears from the present. We see the colors of the early–type cluster members become bluer with increasing redshift as expected from a passively evolving stellar populations. We fit a set of models to the change in the color as a function of redshift with the best fitting values ranging from a formation redshift of 3_{-1}^{+2} to 5_{-3} , depending on the specific model used, though we find no dependence for the formation epoch on the metallicity of the populations. The large scatter in resulting formation epochs, which depends on the details of the models used, implies that we can conclude that the oldest stars in the elliptical galaxies appear to have formed at redshifts of $z > 3$. We find possible evolution in the scatter of the colors, with some high redshift clusters showing scatter as small as the Coma cluster but others showing much larger scatter. Those clusters with a small scatter imply either a formation redshift of at least $z \sim 3$ or a smaller spread in the range of formation redshifts at lower redshifts, assuming a Gaussian distribution of star-formation around the mean epoch.

Subject headings: galaxies: clusters: general — galaxies: elliptical and lenticular, cD, — galaxies: evolution — galaxies: fundamental parameters — galaxies: photometry

1. INTRODUCTION

The color–magnitude relation of galaxies has long been used to study the evolution and formation of elliptical and S0, or early–type, galaxies in clusters (Faber 1973; Visvanathan & Sandage 1977; Sandage & Visvanathan

1978, for example). The canonical picture of the formation of early–type galaxies was the monolithic collapse model of Eggen et al. (1962). In this scenario, elliptical galaxies form through the gravitational collapse of large clouds of gas. As the system forms, it goes through a burst of intense star formation which quickly ends as the majority of the gas in the galaxy is either locked up in stars or heated to extreme temperatures, preventing further star formation. One of the crucial pieces of evidence for this model was the work of Bower et al. (1992), since updated with Terlevich et al. (2001). The authors found a small scatter in the colors of early–type galaxies in the Coma cluster. Such uniform colors for the early–type galaxies implies an early epoch of star formation for the galaxies and small range in the epochs from galaxy to galaxy. Aragón-Salamanca et al. (1993), Stanford et al. (1995, SED95) Ellis et al. (1997) and Stanford et al. (1998, SED98) extended this work to moderate redshifts. In those papers the authors found no evolution in scatter or slope of the early–type galaxy color–magnitude relation. Further, in SED98 and

¹ Based on observations with the NASA/ESA Hubble Space Telescope, obtained at the Space Telescope Science Institute, which is operated by the Association of Universities for Research in Astronomy, Inc. under NASA contract No. NAS5-26555.

² Participating Guest, Institute of Geophysics and Planetary Physics, Lawrence Livermore National Laboratory

³ Presently at Lick Observatory, University of California

⁴ Visiting Astronomer, Kitt Peak National Observatory, National Optical Astronomy Observatory, which is operated by the Association of Universities for Research in Astronomy, Inc. (AURA) under cooperative agreement with the National Science Foundation.

Electronic address: holden@ucolick.org, adam@igpp.uclnl.org

Electronic address: prme@kromos.jpl.nasa.gov

Electronic address: med@stsci.edu

⁵ The Space Telescope Science Institute is operated by the AURA, Inc., under National Aeronautics and Space Administration (NASA) Contract NAS 5-26555.

de Propris et al. (1999), the authors found that the evolution of both the colors of early-type cluster galaxies and the luminosities of all cluster members agrees with passively evolving stellar populations.

The monolithic collapse model was called into question with the work of Kauffmann & Charlot (1998). In their picture, early-type cluster galaxies build up wards from the accretion of smaller systems, a process often referred to as hierarchical merging. Kauffmann & Charlot (1998) were able to recreate the observed color-magnitude relation of cluster early-type galaxies at low redshift with a merging formation model. However, their model alone does not answer the question of how the small scatter in cluster member colors comes about. van Dokkum & Franx (2001) suggest a solution to that problem in the hierarchical merger scenario with the “progenitor bias.” In this model, early-type galaxies form continuously through merging but are only identified as early-type galaxies when star formation has ceased. The selection of an ensemble of early-type galaxies will, therefore, only find the most extreme members of the distribution of star-formation histories in the whole of the galaxy population. Anytime the most extreme members of a random distribution are chosen, the distribution of properties among those members is quite small. Nonetheless, the uniformity of the population of stars in early-type galaxies is such that van Dokkum & Franx (2001) finds that early-type galaxies have more than half of their stars formed at or near the beginning of the star formation epoch. Bower et al. (1998) find a slightly stronger result, requiring that the majority, $\geq 50\%$, of stars be formed within the first four or so gigayears with only residual star formation still occurring at later epochs.

In this paper, we investigate the color-magnitude relation of early-type galaxies in the redshift range $0.58 < z < 1.27$. We focus on six clusters with $0.78 < z < 1.27$, to probe the highest observable redshifts in order to have the most sensitivity to the formation epoch of the stars in early-type galaxies. We present the early-type galaxy color-magnitude relation for these six clusters and quantify the observed evolution in the slope and scatter. In addition, we discuss the evolution in the zero-point, or average color, of the relation. We rely on the data of Stanford et al. (2002) in this work, but review our data reduction procedures in §2 with particular attention paid to how we constructed and merged catalogs of Hubble Space Telescope (HST) imaging and ground based imaging. One of the most difficult problems is reliably morphologically typing high redshift galaxies, even when using HST images. We used two different methods and performed a number of checks to ensure we understand how well we can identify early-type cluster members, all of which is discussed in §3. We compared the observed color-magnitude relations with that of the Coma cluster using the data described in de Propris et al. (1998). The comparison, outlined in §4, was done in a similar manner as SED98. We report our measurements in §4 and then discuss our results in §5.

2. DATA

The eight clusters in this sample represent an extension of the SED98 sample, though only six clusters are used in the final analysis. The aim of this paper is to increase

the sample of SED98 at the highest redshifts. All clusters in this paper are in the redshift range $0.58 < z < 1.27$, and with this sample we triple the number of clusters at redshifts $z > 0.75$ from three in SED98 to a total of nine with ones in this paper. The photometric catalogs are published, along with the data for SED98, in Stanford et al. (2002). Below we will briefly review how we prepared our data and highlight any differences with SED95 and SED98.

2.1. Cluster Selection

Each of the clusters in this paper were selected based on the availability of archival HST imaging and photometry from Stanford et al. (2002). The original sample of Stanford et al. (2002) was constructed to encompass all of the high redshift clusters known at the time of the original survey, 1994 through 1996, regardless of the method used to find the cluster. The clusters in this paper’s sample are from the catalog of Gunn et al. (1986), the Einstein Medium Sensitivity Survey (Gioia et al. 1990; Henry et al. 1992; Gioia & Luppino 1994) or from clusters found in the follow-up of the 3C catalog discussed in Spinrad et al. (1985). The one exception is RDCS 0848+4453 (Stanford et al. 1997), which was found over the course of the SPICES survey (Eisenhardt et al. 2001) but is part of the ROSAT Deep Cluster Survey discussed in Rosati et al. (1998).

The heterogeneous selection of clusters for this paper means that there is a variety of follow-up work. In Oke et al. (1998), four of the clusters in this paper were surveyed to determine cluster membership and velocity dispersions. Two of them, GHO 0229+0035 and GHO 2155+0321 are found to be marginal over-densities at best. This implies that they are unlikely to have a significant number of early-type galaxies above the number expected from just the field population. GHO 0021+0406, discussed in Lubin et al. (1998) as CL 0023+0423, appears to have a number of cluster members, but also a large number of the galaxies in the field appear to be projected along the line of sight. The systems appear to be two groups merging, one with a velocity dispersion of 152_{-33}^{+42} km s⁻¹ and the second with a velocity dispersion of 415_{-63}^{+102} km s⁻¹. A side effect of this is that there will appear to be a large number of galaxies in this system, but as the fraction of early-type galaxies is lower in low density environments, there will be a lower than expected early-type fraction given the number of total galaxies. The final cluster in the sample of Oke et al. (1998) included in our sample is GHO 1604+4329, discussed in Postman et al. (2001) as CL 1603+4321. This cluster has 41 spectroscopically confirmed members and velocity dispersion of 935_{-91}^{+126} km s⁻¹, though no detectable X-ray emission according to Castander et al. (1994).

The remaining clusters of our sample were discovered originally from X-ray selected catalogs or radio surveys. MS1137.5+6625 has X-ray imaging as well as X-ray and optical spectroscopy which is discussed in (Donahue et al. 1999). The gravitational arcs and high X-ray temperature both point to this being the most massive system in this paper. 3C184 was spectroscopically confirmed in Deltorn et al. (1997), with 11 redshifts and a measured velocity dispersion of 634_{-102}^{+206} km s⁻¹.

Finally, in addition to a deep Chandra observation discussed in Stanford et al. (2000), RDCS 0848+4453 has fifteen spectroscopically confirmed cluster members. The color–magnitude relation and the fundamental plane of a subset of these galaxies are discussed in van Dokkum et al. (2001) and van Dokkum & Stanford (2003). It is unlikely that GH0 0229+0035 and GH0 2155+0321 will yield enough early–type galaxies to provide a good statistical sample, and that 3C184 and GH0 0021+0406 may have a large number of interloping galaxies because of their small binding masses and, thus, small implied richnesses.

2.2. Ground based imaging

We obtained optical and near-IR images of the clusters using CCD and HgCdTe array cameras on NOAO telescopes at Kitt Peak in 1993–1996. Our imaging provides multi-wavelength photometric data of uniform quality through a standard set of filters, and we used well-understood photometric systems. These features are particularly advantageous when attempting to systematically investigate the evolution of large samples of faint galaxies over a broad redshift range. The sample of clusters studied here, along with the band passes used, is summarized in Table 1. In the near infrared, atmospheric transmission windows require us to use fixed band passes, so we have imaged through standard J , H and K_s filters. We have not obtained all three filters for every cluster in the sample in this paper, but we do have J and either H or K_s for every cluster in our sample.

The optical imaging was generally obtained in two bands which we have adjusted according to the cluster redshift in order to ensure that they span the $\lambda_0 \sim 4000\text{\AA}$ region in the cluster rest frame. As in SED98, the clusters were divided into redshift ranges for this purpose: $0.45 < z < 0.7$ (V and I bands); and $0.7 < z < 0.9$ (R and I bands) while for our clusters at $z = 0.920$, $z = 0.996$ $z = 1.169$ and $z = 1.273$ the combination of the I and J filters straddle the 4000\AA region. In this paper, we will generally refer to the two pass bands that straddle the 4000\AA region as *blue* and *red*. The former measures rest-frame emission at wavelengths similar to or somewhat bluer than the rest-frame U -band, while the latter corresponds to rest-frame wavelengths roughly from B to V .

We chose the exposure times in all band passes to provide galaxy photometry with $S/N > 5$ for galaxies with the spectral energy distributions of present-day ellipticals, down to ~ 2 magnitudes fainter than the apparent magnitude of a L_* , or $m(L_*)$ galaxy at the cluster redshift. This magnitude also includes the same aperture correction as in SED98 between the total magnitude as measured by FOCAS and the true total magnitude of an elliptical galaxy. This permits us to study galaxy properties over a similar range of luminosities for all clusters in our sample, regardless of their redshift. Our ground based images typically cover a field size of ~ 1 Mpc at the cluster redshift, which is generally larger than that covered by the WFPC2 data used to select the early–type galaxy subsamples (see below). The optical data were calibrated onto the Landolt system wherein Vega has $m_V = +0.03$, and the IR images onto the CIT system wherein Vega has $m = 0$. The typical root mean square error of the transformations is 0.02 in the opti-

cal and 0.03 in the near-IR. The effective angular resolution of the images is $\sim 1.2''$ for our sample. The last column in Table 1, which is labeled as Table Number, refers to which table in Stanford et al. (2002) that contains the photometric catalog for the cluster. We use the same identifiers for the galaxies in this paper as used in Stanford et al. (2002).

2.3. HST Imaging

The HST imaging we used in this work came from a combination of archival data and pointing observations by some of the authors. Most of the clusters were observed in the F814W or F702W bands using the WFPC2 instrument. One cluster, GH0 0229+0035, was observed in F606W and two, RDCS 0848+4453 and 3C210, were observed with the NICMOS Camera 3 in the F160W (roughly an H band) as well as with WFPC2 in the F814W filter. In Table 2, we list the total exposure time and the coordinates of the pointings on a filter by filter basis. The NICMOS F160W observations are listed for each central dither position, with the number of the dither position listed next to the cluster name. Three were necessary to adequately cover the WFPC2 fields for those two clusters. The last column in Table 2 lists the table in this paper where the HST imaging results are listed.

2.3.1. WFPC2 Image Preparation

For a given set of images towards a cluster, all images with centers within $0''.05$ of each other were stacked together. This is less than half a pixel in the WF images. Each of these groupings of images was then combined with `crreject`. The sum of each grouping of images was then registered. We shifted the registered images and then combined them with `crreject`. When at all possible, we used integer shifts. Integer shifts, instead of combining the data with `drizzle`, allow us to use GIM2D as a method of identifying early–type galaxies, which we shall discuss in more detail in §3.1.

We have, after all of the above, an image for each chip. We then combined the data quality files into one final data quality file. Any pixel that was marked in one of the data quality files, even if only partially covered by a shifted pixel, was flagged in the final data quality file. We used this final data quality file as a bad pixel mask in later processing with GIM2D. More recent versions of the GIM2D software allow the use of weight maps, instead of forcing us to flag a pixel as bad in all of the data when it is bad in only one of the images.

In Figures 1 through 8, we plot the mosaic images of the WFPC2 imaging. These mosaics have been geometrically transformed into the coordinate system of the data published in Stanford et al. (2002). In most cases, the PC chip was not transformed. The small area generally meant that very few objects with ground based photometry were observed in the PC chip. For RDCS 0848+4453, however, the deeper imaging ground based data allowed the PC chip to be included in the mosaic. For GH0 1604+4329, one of the three WF chips overlaps with little of the ground based data, and so was not displayed in Figure 5. In each figure, North is up and East is to the left. The dashed grid lines are the same as lines for the images in Stanford et al. (2002).

See holden.fig1.jpg

FIG. 1.— Mosaic of WFPC2 frames for GH0 0229+0035 at $z=0.607$. North is up and East is to the left. The dashed lines represent offsets as measured from the brightest object near the center of the field and are the same lines as used in Figure 29 of Stanford et al. (2002).

See holden.fig2.jpg

FIG. 2.— Same as 1 but for GH0 2155+0321 $z=0.7$. The corresponding image in Stanford et al. (2002) is Figure 31.

See holden.fig3.jpg

FIG. 3.— Same as 1 but for MS 1137.5+6625 at $z=0.782$. The corresponding image in Stanford et al. (2002) is Figure 35.

2.3.2. NIC3 Imaging

RDCS 0848+4453 was observed with the NICMOS Camera 3 in three different pointings. Each pointing was observed with a dither pattern of eight exposures, one of 1344 seconds and seven of 1408 seconds. In Table 2 we list the center position of each dither pattern and the total exposure time. The data were processed using a combination of STScI pipeline routines and custom software. All 24 images were combined into a single mosaic using the “drizzling” method of (Fruchter & Hook 2002). The NICMOS images have a point-spread function (PSF) with full width at half maximum (FWHM) of $0''.22$, primarily limited by the pixel scale ($0''.2$) of Camera 3. The final “drizzled” data were sampled at the resolution of the PC camera, $0''.04$ per pixel.

3C210 was also observed with NICMOS Camera 3 in three different pointings. Each pointing was observed six times for a total of 5248 seconds, four exposures of 896 seconds and two of 832 seconds. The data were reduced using the same procedure as for RDCS 0848+4453. Some of the observations, however, were not usable as it appears that the HST lost lock during the observation. We list the total usable exposure time for each of the pointings in Table 2.

We plot mosaics of the NICMOS images, similar to the WFPC2 mosaics, in Figures 9 and 10. The coordinate system and the dashed lines are the same as in the WFPC2 mosaics as shown in Figures 1 through 8.

2.4. Galaxy Catalogs

For each set of imaging data, we constructed different galaxy catalogs. Each catalog had a different scientific goal. With the ground-based imaging data, we measured the total magnitudes and colors of galaxies. The purpose of the catalogs of the HST data was to identify morphological types.

2.4.1. Ground Based Imaging Catalog

Images in all band passes were co-aligned and convolved to matching point spread functions (PSFs) in order to ensure uniform photometry at all wavelengths through fixed apertures. We detected objects on the K images using a modified version (Adelberger, personal communication) of FOCAS (Valdes 1982). We used the same software to obtain photometry in each band

See holden.fig4.jpg

FIG. 4.— Same as 1 but for GH0 0021+0406 at $z=0.832$. The corresponding image in Stanford et al. (2002) is Figure 37.

See holden.fig5.jpg

FIG. 5.— Same as 1 but for GH0 1604+4329 at $z=0.920$. The corresponding image in Stanford et al. (2002) is Figure 40. The third WF chips does not overlap with much of the ground based data and so was included.

See holden.fig6.jpg

FIG. 6.— Same as 1 but for 3C184 at $z=0.996$. The corresponding image in Stanford et al. (2002) is Figure 41.

through circular apertures with a diameter equal to the twice the PSF FWHM. This aperture was the same angular size for all of the images as we convolved all of our data for each cluster to match the largest PSF for that cluster. These apertures will be used for our color measurements while the total magnitude was measured in the longest available infrared band, K_s or H . These total magnitudes are from the modified version of FOCAS used to detect and measure the fluxes of galaxies. The definition in FOCAS is that the total magnitude is the magnitude within an aperture that encompasses twice the detection area. Simulations with FOCAS, see SED98, show that these total magnitudes are, in general, 0.3 magnitudes fainter than the true total magnitude of the early-type galaxies. We do not, however, correct the total magnitudes in our data for this bias.

The observing methods, data reduction techniques, and photometric methods for our ground-based data set are described in detail in SED95 and Stanford et al. (2002). All photometry has been corrected for reddening using the interstellar extinction curve given in Mathis (1990), with values for $E(B - V)$ taken from Burstein & Heiles (1982). The final photometric catalogs are in Stanford et al. (2002).

2.4.2. WFPC2 Catalog

We used SExtractor v2.1.1 (Bertin & Arnouts 1996) to construct a catalog of each of the HST images. For each image, we used the same threshold for detection (1.5σ of the background and a minimum area of ten pixels) and the same filter, a Gaussian with a FWHM of 1.5 pixels. For SExtractor, the other significant parameter that controls the number of detected objects is the minimum contrast parameter for de-blending. We choose a rather small value of 0.00175 (this is the minimum fraction of total light within the detection isophote that the program requires to form a new sub-object), as compared to the value of 0.005 recommended in (Bertin & Arnouts 1996). The combination of the de-blending contrast chosen and the small convolution kernel meant, in general, irregular looking galaxies will be broken up into sub-components. However, close pairs or trios of nearby galaxies will almost always be broken up into separate objects.

The main purpose of using SExtractor was to create a catalog of galaxies for further post-processing. Therefore, we did not try optimize the detection threshold or

See holden.fig7.jpg

FIG. 7.— Same as 1 but for 3C210 at $z=1.169$. The corresponding image in Stanford et al. (2002) is Figure 42.

See holden.fig8.jpg

FIG. 8.— Same as 1 but for RX J0848+4453 at $z=1.273$. The corresponding image in Stanford et al. (2002) is Figure 43.

See holden.fig9.jpg

FIG. 9.— Mosaic of NICMOS F160W pointings for 3C210, at $z=1.169$. The corresponding image in Stanford et al. (2002) is Figure 42.

de-blending parameters to ensure we found every galaxy in the field. Rather, we are interested in the brighter galaxies that can be reliably morphologically typed and used SExtractor to define those galaxies. We used the `flux_auto` parameter in SExtractor, a flux measured within 2.5 Kron radii (Kron 1980), as a total flux measurement. We then trimmed our galaxy catalog to a no-evolution $m(L_*) + 3$ in the observed HST band after converting the fluxes to magnitudes using the zero-points from Holtzman et al. (1995)

2.4.3. NICMOS Catalog

As with the WFPC2 imaging, we used SExtractor to generate an image catalog for each position. Unlike with the WFPC2 data, we did not combine each pointing for a dither position into one image. Instead we generated a catalog for each of the eight images separately. The catalogs were then joined so that an object found in the reference image, the first image in the dither sequence, was matched with the same object in each subsequent image. To create this catalog, we used SExtractor v2.1.1 with a 2.0σ detection limit and a minimum area of 15 pixels. We choose the fiducial value of 0.005 of the contrast parameter. We tested a large number of values and found little change in the output catalog. We chose these numbers as they maximize the number of detected objects in the resulting catalog.

2.4.4. Merging of catalogs

The ground based catalog and the WFPC2 catalogs had to be merged into a final list of galaxies. The main problem is the very different resolution in the ground based imaging as opposed to the HST imaging. We transformed the coordinates in the HST catalog to those in the ground based catalog. We chose a square with five pixels in the HST, or $0''.5$ for the WFPC2 data and $1''.0$ for the NICMOS, on a side to match objects in the two catalogs. The large size of this box, especially when compared to the resolution of the HST, meant we often had multiple matches in the HST catalog for one object in the ground based catalog. These duplicate matches were culled based on visual inspection of ground and HST images. In Tables 4 through 13 we list the positions of the objects detected in the final merged catalogs. Included are the positions and identifiers from Stanford et al. (2002). In that paper, we list the magnitudes and colors used in this paper. We list the informa-

See holden.fig10.jpg

FIG. 10.— Mosaic of NICMOS F160W pointings for RX J0848+4453 at $z=1.273$. The corresponding image in Stanford et al. (2002) is Figure 43.

tion used to determine the morphological types as well, which will be discussed in the next section.

In Table 3, we summarize the collected catalogs. We list, in addition to the cluster name and redshift, the value of $m(L_{star})$. We use the absolute magnitude for a L_* galaxy from de Propris et al. (1998). Table 3 lists the no evolution $m(L_*)$ magnitude (K or H) for each cluster assuming a $\Omega_m = 0.1, \Omega_\lambda = 0.0, H_0 = 65 \text{ km s}^{-1} \text{ Mpc}^{-1}$ cosmology, to be consistent with the values from SED98. In parenthesis, we also list the $\Omega_m = 0.3, \Omega_\lambda = 0.7, H_0 = 65 \text{ km s}^{-1} \text{ Mpc}^{-1}$ cosmology values for comparison. We list the total number of galaxies brighter than $m(L_*)$ in the merged catalogs. We list the total number of early-type galaxies brighter than $m(L_*)$ as classified by our two different classification techniques discussed next, with a slash separating the two values. For 3C210 and RDCS 0848+4453 our total number of galaxies and our number of early-type galaxies are estimated from the NICMOS catalogs. Finally, we list an estimate of the number of field galaxies. We discuss below how that estimate is arrived at.

3. MORPHOLOGICAL TYPES

3.1. Classifications

We used the high-angular resolution imaging from the HST to determine the morphological types of the galaxies in two ways, by visual typing and using an automated machine-based approach. Two methods were used in order to compensate for the difficulties of consistently morphologically identifying galaxies at high redshift.

One of us (SAS) typed, by eye, all galaxies within the merged HST/ground imaging catalogs. Small images extracted from the SExtractor catalogs of the WFPC2 or NICMOS data were used. Each postage stamp size was based on the isophotal size of the image measured by SExtractor. For RDCS 0848+4453 and 3C210, the images from the drizzled NICMOS mosaic were used in the visual typing when an object fell within the field of view of the data, else the WFPC2 images were used.

For an automated approach, we used the GIM2D package (Simard et al. 2002) in conjunction with the classification scheme of Im et al. (2002). The package, described in Simard et al. (2002), fits a two component model to the two-dimensional galaxy images. GIM2D uses as a galaxy model a de Vaucouleurs law with a fixed ellipticity and an optically thin exponential disk inclined to the line of sight. The only constraints shared between the bulge and disk components of the model is that both have the same center and the same background value. The model is then convolved with a point spread function. The best fitting model is found for the two-dimensional image data by minimizing the χ^2 statistic.

After fitting a galaxy model, we used the classification scheme of Im et al. (2002). In this scheme, galaxies are classified with a T-Type of less than 0 if the fraction of light in the model coming from the de Vaucouleurs component is at least 40% of the total light, and fit residuals

must be less than 8% of the light in the galaxy, as determined by the galaxy model normalization. The residuals are quantified using the two asymmetry parameters from Schade et al. (1995). One parameter measures the fraction of the total symmetric flux while the other measures the fraction of the total asymmetric flux in the residuals. Im et al. (2002) add the two which yields the fraction of flux in the residuals compared with the total amount of light in the object. This fraction is measured within two half light radii. Generally, if the residual fraction is smaller than 8% for a galaxy with a bulge fraction greater than or equal to 40%, the galaxy is classified as an early-type. There is an adjustment for the half-light radius of the model, where for small half-light radii, less than three pixels, the fraction of flux allowed in the residuals becomes 7%; see Im et al. (2002) for details on the classification and the simulations used to calibrate these criteria.

Because the classification scheme relies on the amount of residuals, after removing a model which assumes a constant background, this approach is sensitive to close neighbors or galaxies with extended envelopes. For MS 1137.5+6625, we removed the brightest cluster member first, using the best fitting model from GIM2D, and then reran SExtractor and GIM2D to process the remainder of the cluster. Removing other bright galaxies from MS 1137.5+6625 did not change the results of the GIM2D fits, because only the brightest galaxy has the kind of extended envelope found in the most luminous of cluster elliptical galaxies.

For the RDCS 0848+4453 and 3C210 NICMOS imaging, along with the F814W PC data for RDCS 0848+4453, we used a different routine. A specially modified version of GIM2D was used that simultaneously fits a model to the different images for a given pointing, eight for RDCS 0848+4453 and up to six for 3C210. The fitting program then minimizes the χ^2 statistic for all of the images simultaneously. For the NICMOS data, the variance maps, constructed for the drizzled images, were used to construct variance maps for the model fitting. To determine the early-type galaxies, the same parameters were used, the bulge to total ratio, half-light radius and the sum of the residuals, as described above. The only difference was that the residuals were computed on an image by image basis, so we compared the average residuals with maximum values given in Im et al. (2002).

For Table 3, we list an expected number of field early-type galaxies. One of the difficulties is that there does not yet exist a large published sample of early-type members with high resolution infrared imaging at high redshift. Instead, we use the sample of Im et al. (2002). This has two advantages. First, it uses the same automated identification process that our paper uses. Second, it contains a large sample, 145 objects in total. The only disadvantage is that the sample does not go faint enough to reach $m(L_*)$ for the highest redshift clusters in our sample. We augment the sample using the rest of the Groth Strip Survey from Simard et al. (2002). To select potential early type galaxies, we use the same parameters as Im et al. (2002) did for the faintest magnitude bin. This selection process will yield an unknown number of contaminants. However, we go only $\simeq 1$ magnitude below the limit of Im et al. (2002) at the highest redshift. In addition, we use a color cut. We select galaxies red

ward of the color of the bluest early-type galaxy in each cluster field. This should eliminate many of the contaminants in our morphological selection. In general we compute the number of early-type galaxies expected for three WFPC2 chips. For both 3C210 and RDCS 0848+4453, however, we provide the expectation value for the NICMOS pointings, which are 0.42 the size of the WFPC2 pointings. For GH0 1604+4329, we rescale by two-thirds the expected number because we only use two of the three WF chips.

The morphological types are listed in Tables 4 through 13. Each table lists in the first column an identification number which corresponds to the identifier used in the photometric catalogs presented in Stanford et al. (2002). The second and third columns list the offsets, in arc-seconds, in both right ascension and declination from the central cluster galaxy. These positions are the same as used in Stanford et al. (2002). The fourth column corresponds to the morphological class assigned by visual inspection. For Tables 4 through 9, the morphological types are T Types (de Vaucouleurs et al. 1991) where an early-type galaxy is classified as -5 through -1, with 0 being classified as S0/Sa and not included as an early-type galaxy for this paper. Values smaller than -5 are classified as stars. Tables 10, 11, 12 and 13 list a number from zero to five instead of a T Type. A zero represents a star, one represents an early-type galaxy and larger values are for steadily less symmetric systems. We made this change because we could not classify the galaxies reliably on the T Type scale. Instead, we use broad bins for classification. The numbers can be translated, using a value between -5 and -1 for galaxies labeled with a 1.

The next three columns in all of these tables represent the values from GIM2D used to classify the galaxy; the bulge to total ratio, the fraction of the total galaxy light in the residuals, and the half-light radius in arc-seconds. For some objects, the fraction of galaxy light is strongly negative, such as -199.98. This comes from bright stars where the cores have been removed by the cosmic ray rejection algorithm. Fainter stars can usually be identified by a half light radius with a size of less than one pixel, or $0'.1$ for the WFPC2 data. The final columns contain the identification of the galaxy in the HST imaging. For the WFPC2 data, this is the chip the galaxy was in and the position on the chip in pixels. For NICMOS data, we list the pointing number along with the position. The pointings are identified as one, two or three and the numbers correspond to those listed in Table 2.

Two entries in Table 7 have a -1 in every GIM2D column. These galaxies were too close to the edge of the WFPC2 frame for GIM2D to fit a model but we could determine visual classifications. Table 5 lists object #8 twice. It is clearly separated into two objects in the HST frame but is a blend in the ground based image. Table 12 lists object #6 three times as it was de-blended into three separate objects in the WFPC2 data. In the NICMOS data, however, it remains one object. Object #6 is a confirmed cluster member and possible merger candidate, see van Dokkum et al. (2001) for further discussion.

3.2. Comparing visual types with GIM2D

We plot in Figure 11 examples of early-type galaxies. We have plotted six galaxies, with a magnitude within 0.2

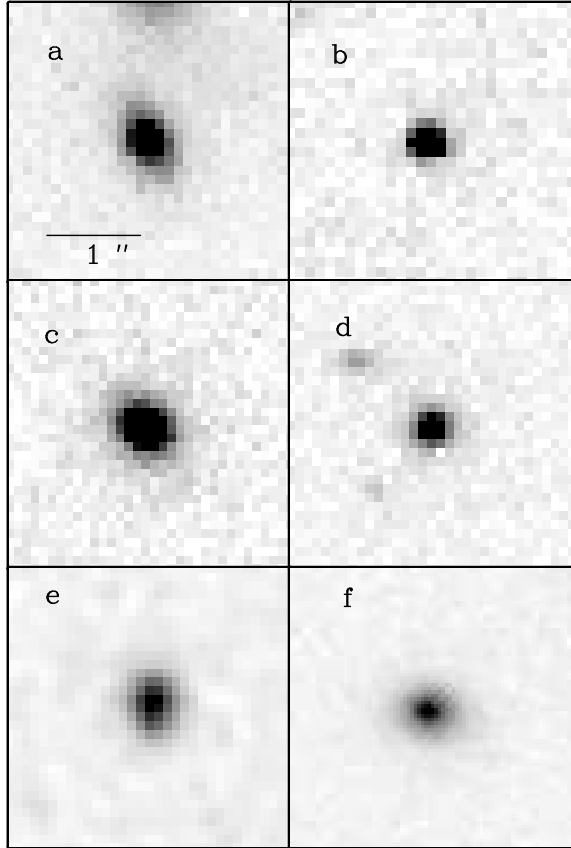


FIG. 11.— Six early-type galaxies, all within ± 0.2 magnitudes of $m(L_*)$, are plotted. Each galaxy is classified as an early-type visually and by using GIM2D. Each galaxy image is the same angular size, a solid line in part a is provided for scale. a) Object # 57 (194,270) from MS1137.5+6625, classified as -1. b) Object # 57 from GH0 0021+0406, classified as a -5. c) Object # 62 from GH0 1604+4329, a -3. d) Object # 19, a -2 from 3C184. e) Object # 50 from the NICMOS imaging of 3C210. f) Object # 43 from the NICMOS imaging of RDCS 0848+4453. The images for e and f were both based on drizzled data, though the GIM2D models were not fit to that data.

magnitudes of $m(L_*)$ that was classified as an early-type by both visual inspection and by GIM2D. Each postage stamp has the same field of view, $3''.2$, and we plot in one figure a $1''.0$ bar for scale. Two of the galaxies are from the NICMOS imaging, one from 3C210 and one from RDCS 0848+4453. Both stamps are drizzled images, and therefore not the images we used for GIM2D fits. The 3C210 image has pixels of $0''.1$, as do all of the WFPC2 images. The RDCS 0848+4453 data was drizzled to a scale of $0''.04$ so as to match up with the pixel scale of the PC chip.

For a comparison between the approaches to morphological classification, we used our results for MS 1137.5+6625. This cluster is a rich, compact system at a redshift of $z = 0.78$ (Gioia & Luppino 1994; Clowe et al. 1998; Donahue et al. 1999) with a large number of early-type galaxies in the cluster for which we can compare classifications. The visual classifications for MS 1137.5+6625 yielded 37 early-type galaxies while the automated classification system yielded 35 early-types. Of the 37 visually classified galaxies, 10 are not classified

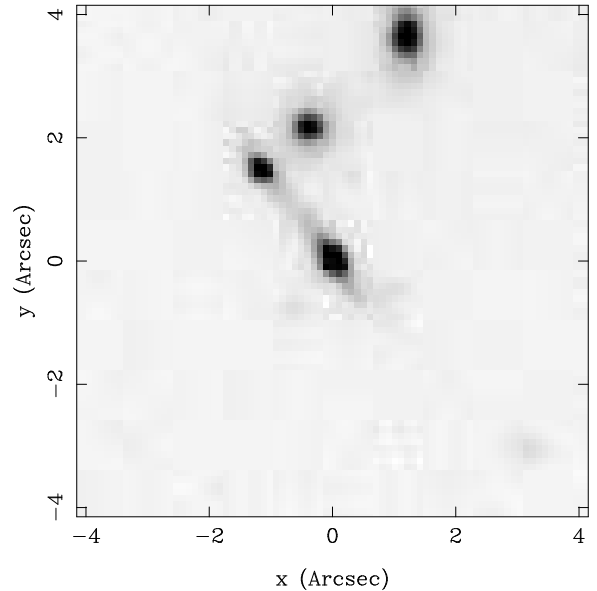


FIG. 12.— The brightest early-type galaxy, object # 11 in Table 6, as classified by SAS but not by GIM2D in MS 1137.5+6625. In the ground-based image the galaxy in the center is blended with the galaxies to the north.

as early-type galaxies by GIM2D.

The galaxies classified visually as early-type galaxies but not classified as such by GIM2D fall into three categories: galaxies classified as early-type spirals by GIM2D (two), galaxies with close neighbors (five) and edge-on galaxies (three). The brightest galaxy classified by SAS as an early-type but not classified as such by GIM2D is in Figure 12 (#11 in Table 6). This is a complicated system with three galaxies very close on the sky and is possibly lensed. Nonetheless, this makes a good example of the first type of discrepant object, one with a bright, nearby companion. Most of the clusters in this sample are much less rich and compact when compared with MS 1137.5+6625. So, the errors in the automated classification caused by image crowding should be less pronounced and there should be fewer edge-on galaxies, as they only make up small percentage of the over-galaxy population. The second kind of discrepant object can be seen in Figure 13 (#40 in Table 6). The galaxy is an isolated object classified as a S0 by SAS. The best fitting model is bulge dominated, with a bulge to total fraction of 0.74, but with residuals that make up 11% of the total flux. The residuals are anti-symmetric, having large positive values in one half of the galaxy and large negative values for the second half. Such residuals are an artifact of an absorbing material, such as dust, which would depress the flux from the galaxy center. This cause the best fitting model to be offset in the centroid from the center of the galaxy, causing this particular set of residuals. Therefore, the visual classification is likely correct as there are S0 galaxies with small dust lanes observed at the present epoch.

There are eight galaxies not classified as an early-type by visual classification but meet the criteria from GIM2D. Of these eight, three are classified as T Type 0, or S0/Sa, three are T Type 1 or a Sa and two are T Type

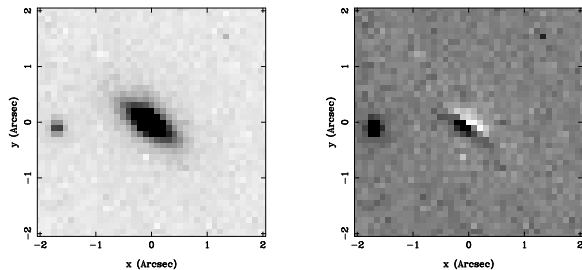


FIG. 13.— In the left panel is object # 40 in Table 6, a S0 according to SAS, with a GIM2D bulge to total ratio of 0.74 but with large model residuals. The residuals are plotted in the right panel.

2 for Sa/b. As all are visually classified as early-type spirals, we conclude that the discrepancy comes from the scatter in galaxy classification technique, inherent in any measurement. A further confirmation of this comes from examining those galaxies which have colors in agreement with galaxies classified as early-types but have T Types of greater than 0 according to the automated classification. We use the 27 early-type as classified by GIM2D to determine a color-magnitude sequence. Ten late-type galaxies have colors similar to this color-magnitude sequence. Of these ten late-type galaxies, none has been visually classified to have a T Type greater than 2.

3.3. Comparing GIM2D with the Medium Deep Survey

Lubin et al. (1998) use the automatic object detection and classification methods of the Medium Deep Survey (Ratnatunga et al. 1999, MDS) to quantitatively analyze the morphology of GHO 0021+0406. The approach of the MDS is similar to what we have done in that the pipeline consists of a two step process, an object detection step and an object classification step. For the MDS, object detection is done by looking for contiguous pixels with a signal to noise of 1σ in the WFPC2 image. The MDS team then makes an object mask and uses the masked image to determine the pixel associated with a given object. The object classification step begins with a simple moment analysis of the pixels in a given objects mask, then proceeds with a maximum likelihood fit to the object pixels of a model.

Though the methods used by the MDS are quite similar to the SExtractor and GIM2D analysis we have performed, there are two main differences. First, we chose, in SExtractor, a very small number for the de-blending parameter, knowing that we would separate galaxies with complicated morphologies into several smaller objects (see §2.4.2). We chose this approach because we wanted to use the asymmetry parameters and we wanted to ensure that objects projected into the line of sight of early-type galaxies would be de-blended in most cases. In contrast, the MDS team de-blends in a much less stringent manner, to prevent flocculent spirals or other galaxies with internal structure from being de-blended into multiple objects. The second major difference is that the MDS team did not fit a full bulge plus disk model to all of the objects as we did. Only those objects with a total signal to noise above a certain threshold were fit (Ratnatunga et al. 1999). Also, if a galaxy was almost as well fit by a pure bulge or pure disk model, that model

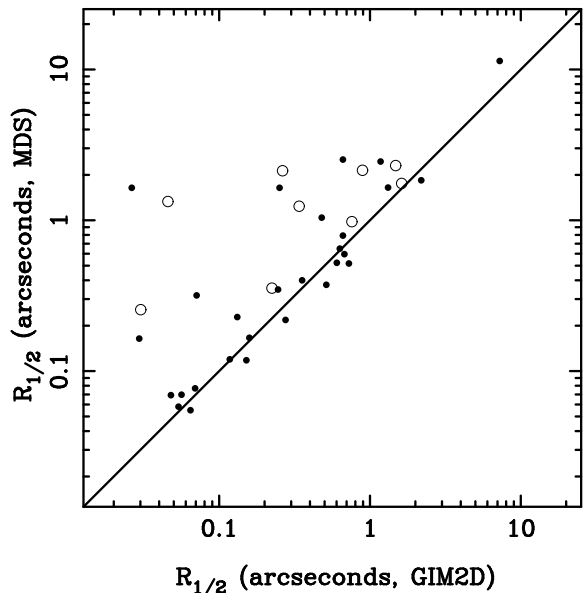


FIG. 14.— The logarithmic half-light radius as measured with GIM2D as compared with the Medium Deep Survey values for GHO 0021+0406. Solid points represent galaxies where SExtractor found only one object within $1''$, open circles are galaxies where more than one object from the SExtractor catalog was within $1''$ of the MDS centroid. The line is a one to one relation, not a fit. See §3.3 for further details.

was used in place of the combined model.

For GHO 0021+0406, we compare the galaxies where the MDS fit a full bulge plus disk model to our resulting models using GIM2D. First in Figure 14 we compare the half-light radii of the two approaches. The solid dots are galaxies where, in the process of matching the SExtractor catalog and the MDS catalog, there was only one galaxy in the SExtractor catalog within $1''$ of a MDS galaxy. The open circles represent where two or more galaxies from the SExtractor catalog were within $1''$ of a MDS galaxy. We then chose the galaxy in the SExtractor catalog with the smallest separation from the MDS galaxy. Clearly there is a tendency for larger half-light radii from the MDS results. Based on the scatter in the open circles, most, if not all, of the discrepancy between the two sets of model fits must come from the very strict de-blending approach we used in creating the SExtractor catalogs.

In Figure 15, we plot the ratio of the bulge flux to the total flux, where total is defined as the bulge model flux plus disk model flux, for the two samples. We use the same symbols as in Figure 14. The MDS results in general agree with the GIM2D results. However, a few of the galaxies seem to have values of the B/T ratio that are quite different when comparing the two algorithms. Unlike with the half-light radii, this does not seem to depend on the criteria used to de-blend objects in the SExtractor catalog.

In Figure 15, we place boxes around two data points with strongly discrepant bulge to total ratios. In Figure 16 we plot these galaxies along with their surface brightness profiles as determined by the IRAF task `ellipse`. The object in the upper left of Figure 16 was classified by GIM2D to have a bulge to total ratio of 0.18 ± 0.02

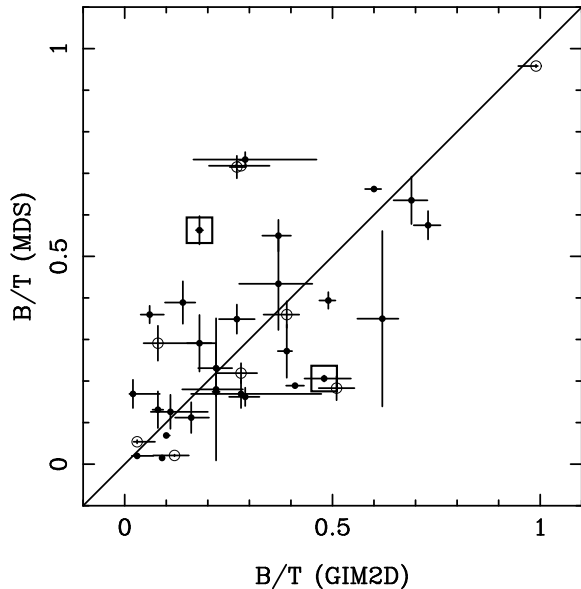


FIG. 15.— The bulge to total ratio as measured with GIM2D as compared with the Medium Deep Survey values. We use the same symbols as in Figure 14. The line is a one to one relation. The two galaxies represented by boxes are shown in Figure 16 and discussed in §3.3.

while the MDS classified it to have a bulge to total ratio of 0.56 ± 0.03 . Based on the surface brightness profile in the upper right of Figure 16, it is clear that the spiral structure in the galaxy, along with an inner ring, cause multiple breaks in the surface brightness profile. These breaks no doubt allow multiple models to be fit. The second object with a box in Figure 15 is in the lower left of Figure 16. GIM2D fits a bulge to total ratio of $0.48^{+0.15}_{-0.11}$ while the MDS yields 0.206 ± 0.007 . This galaxy is classified as an early-type by GIM2D, as the model residuals are 1% of the galaxy flux. This object was visually classified as a -3 in this paper and an “E/Sa?” by visual inspection in Lubin et al. (1998). Clearly the extended envelope makes visual and automated classification problematic. We shall however, consider the object an early-type galaxy as both GIM2D and our visual classification yield a consistent result.

3.4. Comparing GIM2D with Simulations

We used the sample of Frei et al. (1996) to create simulated HST galaxy images. For every cluster, a blank piece of sky was extracted from the imaging data. For RDCS 0848+4453 and 3C210, both a frame from the WFPC2 F814W and from the NICMOS data were used. Each galaxy from Frei et al. (1996) was imaged in multiple bands. For the simulations, we choose the band closest to the observed HST band at the appropriate redshift. For example, for RDCS 0848+4453, we used the B_j band or the g band images from the Frei et al. (1996) catalog when simulating the WFPC2 F814W data and the R or r images when simulating the NICMOS F160W data. This has the effect of adding some morphological changes expected when observing the same galaxies in different filters. Once a filter was chosen, the image size was as appropriate for the redshift of the cluster in our assumed cosmology. For the local dis-

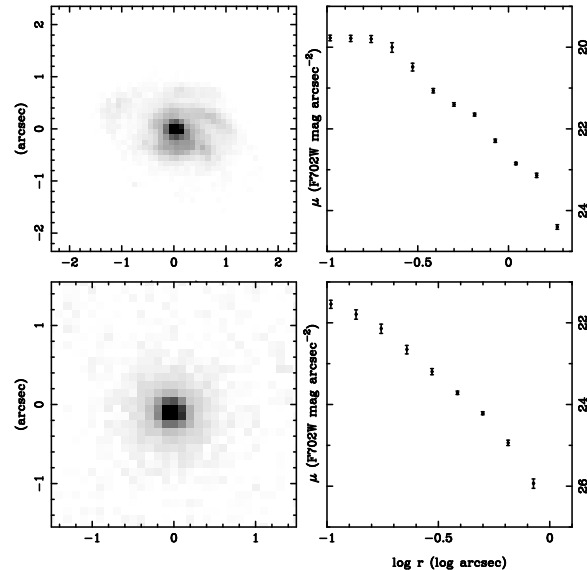


FIG. 16.— The two galaxies plotted with open squares in Figure 15. The top galaxy was assigned a high bulge to total ratio by the MDS and a low value by GIM2D, thus it lies above the line in Figure 15. The bottom galaxy was assigned a low bulge to total ratio by the MDS and high value by GIM2D.

tances of the Frei et al. (1996) catalog, we used the HST Key Project to Measure the Hubble Constant distances (Freedman et al. 2001), when available and, additionally, assumed that all members of the Virgo cluster were at the same distance. In addition, we used the results of Tully & Pierce (2000) and the distances in Giraud (1998) (see references therein.) If we did not find a distance in the literature for a given galaxy, we instead used the redshift as a proxy measurement for the distance to the galaxy. After rescaling, each image was convolved with an appropriate point spread function. The magnitude of the galaxy was fixed at a number of different levels starting from $m(L_*) - 1$ at the redshift of the cluster in the observed band to $m(L_*) + 2$, spaced at half magnitude intervals. The pixel values for the fake galaxy were then used as expectation values for Poisson random deviates. The data were then divided by the appropriate gain for WFPC2 and the noisy, fake galaxies were added to the blank piece of sky from each cluster’s image. The data reduction pipeline was run on this resulting image using the same SExtractor and GIM2D configuration files as used for the original cluster imaging data.

The automated classification process consists of two components, measuring the bulge-to-total ratio and measuring the flux in the residuals. The half-light radius is a third component, but only affects the results in a minor way. Overall, for the WFPC2 simulation, we found that the average error in the bulge to total ratio was around 5% at $m(L_*) - 1$ to 30-40%, depending on the cluster, at $m(L_*) + 2$. Therefore, at $m(L_*) + 2$, a galaxy with a true bulge to total ratio of 50% would have a measured value of 10% or less, 16% of the time. At $m(L_*)$, the error on the bulge-to-total ratio was around 10% or less. As we are most interested in measuring the color-magnitude relation of $m(L_*)$ or brighter galaxies, this means that most of them have reliable bulge to total ratios. When we

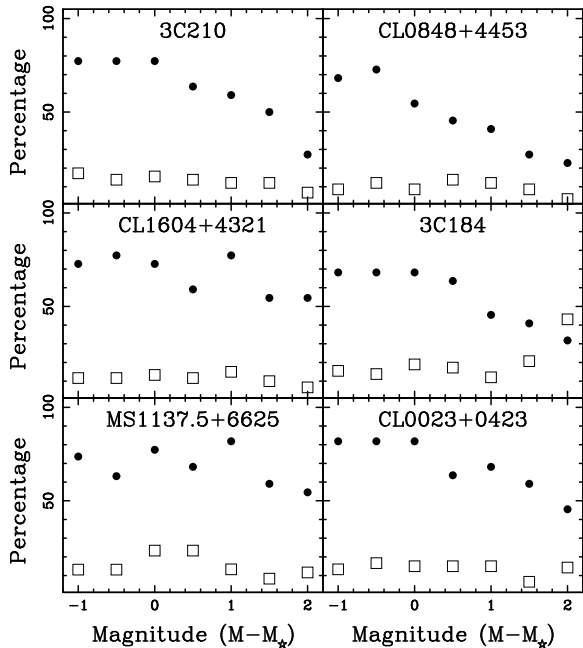


FIG. 17.— We plot, for each cluster where we used the WFPC2 imaging for automatic classification, the fraction of correctly identified early-type galaxies in our simulations as solid points. As open squares, we plot the fraction of late-type galaxies incorrectly identified as early-type galaxies from our simulations.

compare these simulations with the classifications done using the bulge to total ratio and the size of the residuals, this conclusion is borne out. At $m(L_*)$ or brighter, around 80% of the galaxies in WFPC2 are correctly classified as early-type galaxies. The correct classification rate drops to around 40% at $m(L_*) + 2$. Given the large errors on the bulge to total ratio at these magnitudes, this result is not surprising. We plot our results, on a cluster by cluster basis, in Figure 17. In that Figure, we plot both the false positive rate, with open squares, and the fraction of total early-type galaxies classified, using solid circles.

For RDCS 0848+4453, we found significantly worse results when using the WFPC2 data for classification. The best correct classification rate, $\simeq 70\%$, occurs at magnitudes brighter than $m(L_*)$ with a rate of 55% at $m(L_*)$. The false positive rate at these magnitudes is around 9%. There are five early-type galaxies brighter than $m(L_*)$ according to the GIM2D classification scheme, which means it is likely that there are seven or eight in the cluster. At faint magnitudes, the correct classification rate drops to 20% at $m(L_*) + 2$. A large part of this comes from the much worse errors on the bulge to total ratio, usually double the size reported for the lower redshift clusters at the same magnitude. No doubt this is a result of the faint magnitudes and therefore low signal-to-noise for cluster galaxies at this redshift.

Both RDCS 0848+4453 and 3C210 were observed and classified with NICMOS F160W imaging as well. Similar simulations were performed for the NICMOS data as well. Instead of a single noisy, fake galaxy being used for each simulation, one was constructed for each dither position and it was added to an oversampled image. Small

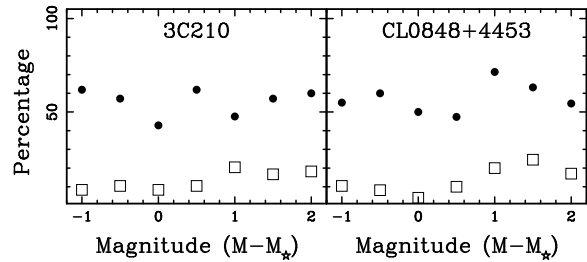


FIG. 18.— We plot, for each cluster where we used the NICMOS F160W imaging for automatic classification, the fraction of correctly identified early-type galaxies in our simulations as solid points. As open squares, we plot the fraction of late-type galaxies incorrectly identified as early-type galaxies from our simulations.

random errors were added to the true dither offsets to simulate our uncertainties in the observed offsets between the observed images of a given galaxy. After a galaxy image was oversampled, it was convolved with an oversampled point spread function made by TinyTIM. This image was binned up to the resolution of the instrument and then added to a noisy frame of from the actual NICMOS imaging data from a given observation.

In Figure 18 we plot the classification rate and false positive rate for the NICMOS observations of RDCS 0848+4453 and 3C210. We find a good rate of success for RDCS 0848+4453, roughly a $\sim 65\%$ classification rate at most magnitudes, which is better than we found for RDCS 0848+4453 in the F814W data. For 3C210, we also find an almost constant classification rate as a function of magnitude as well. For 3C210, however, the highest classification rate is never as high as that for the WFPC2 imaging data. For both clusters the false positive rate grows at fainter magnitudes, as expected. However, we note that the classification rate for both clusters is flat as a function of magnitude, which we did not see in the WFPC2 simulations. There are two reasons for this. First, the NICMOS data observes the rest-frame R band of the early-type galaxies, where the light from the older stellar populations found in bulge systems dominates. None of the WFPC2 imaging for these two clusters sampled as red a part of the spectral energy distribution, but rather sampled the rest frame B or U band which is more sensitive to recent star formation. Second, the lower resolution of the NICMOS Camera 3 data means that, even with dithering, the data are less sensitive to smaller bulges. These two effects compete, making it easy to detect bulge dominated systems in the NICMOS imaging data, but only when the bulge size is sufficiently large to be well resolved. As a result of these effects, we find our success rate for identifying pure elliptical systems is 10% to 20% higher in our NICMOS simulations than our rate for S0 galaxies, where the bulges are smaller. We also find that our success rate for S0 galaxies falls off, as expected, with fainter magnitudes. These results mimic the greater success rate for pure elliptical systems that is found in Im et al. (2002).

Using the simulations of the automated identification process, as shown in Figures 17 and 18, we only counted galaxies with magnitudes $m(L_*) + 0.6$ or brighter when computing the early-type fraction. For most clusters, the false positive identification rate is around 10% to 20%,

while the success rate is around 70%. This yields a couple of galaxies per cluster falsely identified as early-types and slightly more galaxies per cluster missed. Therefore, our estimates of the early-type fraction are, at most, underestimated by 20% of the total number of galaxies. This should not significantly bias our measures of the color evolution of our sample.

4. MEASURING EVOLUTION IN THE COLOR-MAGNITUDE RELATION

4.1. *The Coma No-evolution Prediction*

We compared our high redshift cluster color-magnitude relations with that of Coma, using the data from de Propris et al. (1998) and Eisenhardt et al. (2004). For each cluster, we transformed the Coma photometry into the observed bands.

First, we have to take into account the different sized apertures used for the two data sets. The apertures used for the Coma photometry were fixed to be $24''$, or a $12''$ radius, while the apertures used when measuring the cluster photometry were fixed angular apertures, which are listed in Stanford et al. (2002). We used the color gradients of Coma from Stanford et al. (1998) to correct the Coma colors to the aperture used for the high-redshift cluster galaxies. Scodreggio (2001) raised a potential bias in measuring the color-magnitude relation. Early-type galaxies become bluer at larger radii so, unless measuring at the same apparent radii, we could detect a spurious signal of evolution. By using the color gradients to correct all color measurements to a common physical radius, we should compensate for this bias.

We transformed the Coma data to the observed frame of the cluster. We did this transformation by choosing the two Coma filters that, when placed at the redshift of the cluster, are the best match for the filter used for that cluster. We then calculated the bandpass correction, the zero-point correction and the small k-correction for that filter to transform into the observed filter. Below we show the equation we fit,

$$F_z = F_{c,1} + x * (F_{c,1} - F_{c,2}) + C$$

where F_z is the filter we wish to transform the photometry to, $F_{c,1}$ represents the filter for the Coma photometry closest, when shifted, to the output filter, $F_{c,2}$ is the second closest filter, x represents the magnitude of the color term and C represents the small k-correction and the difference in zero-points between the two filters. To calculate these, we used two spectral energy distributions, a present day early-type galaxy as represented by a 10 gigayears old model galaxy from Bruzual & Charlot (1996), though based on Bruzual & Charlot (1993), and a slightly bluer galaxy, with colors similar to a typical Sa galaxy, also from Bruzual & Charlot (1996). We passed these spectra through the Coma filters and calculated the expected fluxes. We then red-shifted the spectra to calculate the expected flux in F_z and solved the above equation for C and x . Each Coma galaxy was transformed by the above equation to have its magnitudes predicted for the filters of the high redshift clusters.

The filters used for the cluster observations were chosen to match as well as possible the low redshift U and B or V filters. Clusters observed near edges of the redshift ranges described in 2.2, however, may require a small extrapolation to match the observed Coma data to the high

redshift cluster observations. The largest extrapolation in this regard is RDCS 0848+4453 where the I samples 3550 \AA , 200 \AA blue-ward of the central wavelength of U at the redshift of the Coma cluster.

To compute the transformed Coma galaxy colors, we use two templates that were chosen to match the colors of either an early-type, $m(L_*)$ galaxy or a red, $m(L_*)$ spiral, in Coma. Nonetheless, the templates were chosen from the Bruzual & Charlot (1996) models. The selection of the particular templates is a source of error in the color transformation. For example, for RDCS 0848+4453, we had to extrapolate the rest-frame ultraviolet flux in order to compute the predicted no-evolution $I - J$ color. To estimate the size of this error, we used the Coleman et al. (1980) templates, specifically the elliptical galaxy and the Sbc template. The elliptical galaxy template of Coleman et al. (1980) predicts bluer colors for Coma than we observe, possibly because it was constructed from the bulges of nearby Spiral galaxies, rather than true elliptical galaxies.. Nonetheless, in most cases, we find a small change, $\simeq 0.05$ magnitudes, in predicted colors of Coma cluster galaxies when using the templates of Coleman et al. (1980) versus the Bruzual and Charlot model mentioned above. This value is around the same size as the uncertainty in the zero point of the Coma photometry, $\simeq 0.02$ in the optical pass bands and $\simeq 0.03$ in the infrared pass bands, or $\simeq 0.04$ magnitudes in the optical - infrared colors. These terms, along with PSF matching errors, extinction correction errors and the color-gradient corrections, all total an systematic error of 0.06 magnitudes, which is further described in SED95.

4.2. *High Redshift Color-Magnitude Relations*

We plot in Figures 19 through 28 the color-magnitude relations for the early-type galaxies in the clusters in our sample. For each cluster, we plot three color-magnitude relations, the two straddling the 4000 \AA break and $J - H$ or $J - K$ relation. We compare these colors with the total magnitudes measured in either the H or K bands. For each diagram, we plot two sets of points. The open circles represent early-type galaxies as identified using GIM2D (see §3.1) while the solid points are those visually identified (see §3.1). We also plot three lines for each diagram. The solid line corresponds to the transformed no-evolution prediction from the Coma data discussed above. The dashed line represents the fit to the color-magnitude relation for the galaxies identified by GIM2D while the dotted corresponds to the fit for the visually identified galaxies. In two cases, GHO 0229+0035 shown in Figure 19 and GHO 2155+0321 shown in Figure 20, there were only a few early-type galaxies identified by GIM2D or by visual inspection, so we performed no linear fits. After comparing the number of observed early-type galaxies to the number of predicted early-types, see Table 3, it is entirely consistent that there is no cluster of early-type galaxies in either case, but rather we are simply seeing the field ellipticals population. For the remainder of this paper, we will not use the results from these two clusters. Figure 27 shows the GIM2D classifications for RDCS 0848+4453 based on the WFPC2 F814W data. These data sample the rest frame ultra-violet at the redshift of this cluster and for 3C210. This part of the spectrum does not sample well the older stellar popula-

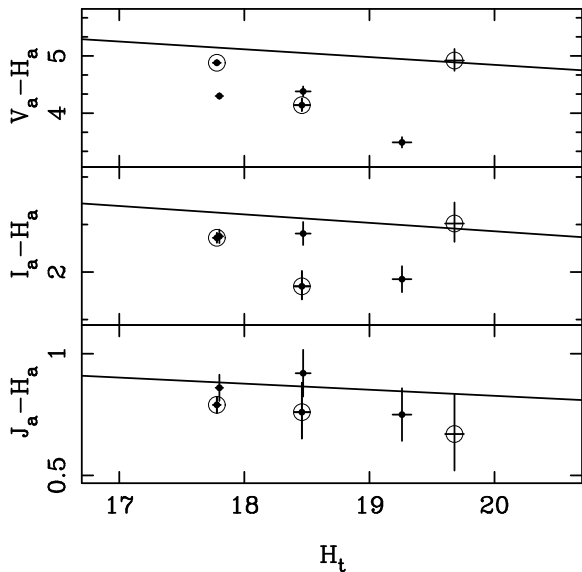


FIG. 19.— Color-magnitude diagrams for the cluster GH0 0229+0035 at $z=0.607$. The colors, based on aperture magnitudes are plotted versus the total magnitude for the early-type galaxies in cluster. Galaxies are represented by solid dots if visually typed or by open circles if identified by the bulge-disk model fits. The solid line is the color-magnitude relation of the Coma cluster of galaxies transformed into the observed filters. Values with the subscript “a” are measured within a fixed angular aperture where all of the images have been smoothed to the worst seeing, the aperture radius is given in Table 1. Values with the subscript “t” are the total magnitudes of the galaxies, as measured with FOCAS. See 2.2 for a discussion of the total magnitudes and how they relate to “true” measures of the total flux from an early-type galaxy.

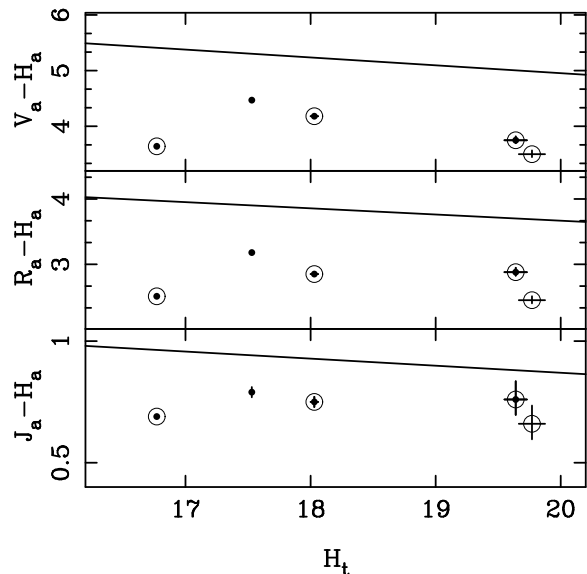


FIG. 20.— Same as Figure 19 but for GH0 2155+0321 at $z=0.7$.

tions that dominate bulges of galaxies and, therefore, the simulations in §3.4 show a low rate of correct morphological classification. For the rest of this paper we only use the morphological classifications for RDCS 0848+4453 based on the NICMOS data presented in Figure 28. For 3C210, we will use both the WFPC2 and the NICMOS data because of the short exposure times in some of the NICMOS imaging, see §2.3.2.

When fitting the color-magnitude relation, we first restricted the range of total magnitudes to only those brighter than $m(L_*) + 2$; see Table 1 for the values of $m(L_*)$ we used. We then calculated the biweight location and scale of the colors (Beers et al. 1990). If a galaxy was more than *two* scale lengths, two standard deviations for a Gaussian distribution, from either side of the peak in one of the color-magnitude relations, it was removed from the early-type sample. In addition, we removed all galaxies more than half a magnitude from the biweight peak $J - K$ or $J - H$ color and more than one σ redder than the expected no-evolution result. All galaxies used in the fit are shown in the plotted color-magnitude diagrams in Figures 21 through Figure 28.

To fit the color-magnitude relation, we used the bivariate correlated errors and intrinsic scatter (BCES) estimator from Akritas & Bereshady (1996) as implemented in the software provided by the authors. Specifically, we followed the recommendation of Akritas & Bereshady (1996) for fitting the color-magnitude relation and used the BCES($X_2|X_1$) estimator. This technique requires an estimate of the error for both the color and magnitude

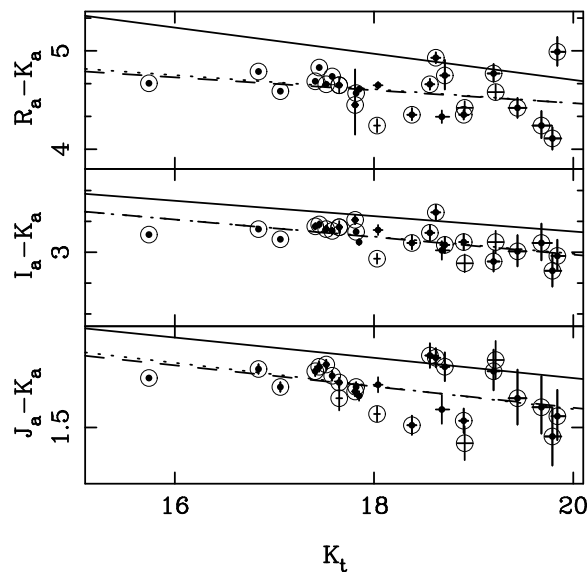


FIG. 21.— Same as Figure 19 but for MS 1137+6625 at $z=0.782$ with the addition of a dotted line which is the fit to the visually identified early-type galaxies and a dashed line which is the fit to the automatically identified early-type galaxies.

as well as the covariance between the color and magnitude. We estimated the errors on our magnitudes by a series of simulations described in SED98. As the color term depends on the magnitude, there is a strong covariance. We simply used the errors in the aperture magnitudes for whichever magnitude was a total magnitude, K or H , as our estimate of the covariance as was done in Akritas & Bereshady (1996). In Figure 29, we plot the difference in the slopes, specifically we subtract the Coma slope from the observed slope, such that a flatter slope will have a positive value in the figure.

As with SED98, we will also probe the evolution in the stellar populations of early-type galaxies using the

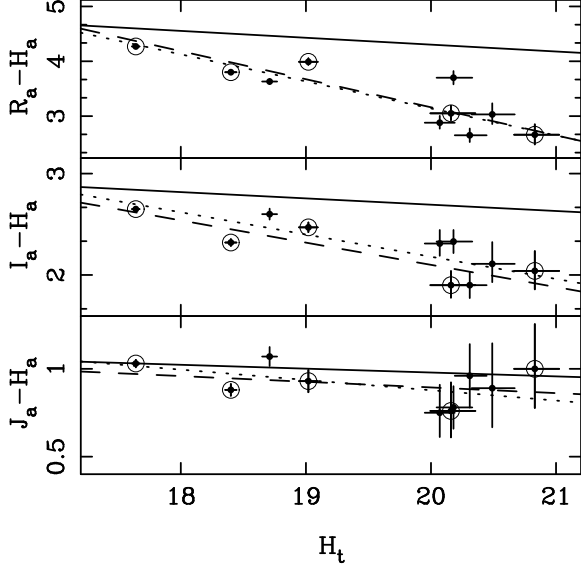


FIG. 22.— Same as Figure 19 but for GH0 0021+0406 at $z=0.832$.

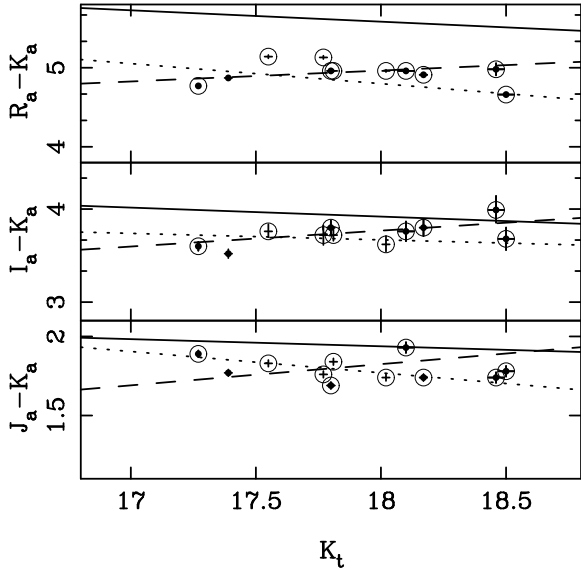


FIG. 23.— Same as Figure 19 but for GH0 1604+4329 at $z=0.920$.

offset of the color-magnitude relation from the Coma no-evolution prediction. In Figure 30, we plot the offset of the color-magnitude relation for the early-type galaxies in the clusters as a function of redshift. This offset we calculated by computing the y-intercept that best fit the data assuming the slope of the Coma no-evolution relation. We note here that, unlike in SED98, for GH0 1603+4313 we chose the I filter to represent the “blue” and the J to represent the “red” for these figures only. This is necessary for comparing with the models described below.

Finally, we calculate the scatter in the colors around the color-magnitude relation. For our estimate of the scatter, we use the biweight scale of the early-type galax-

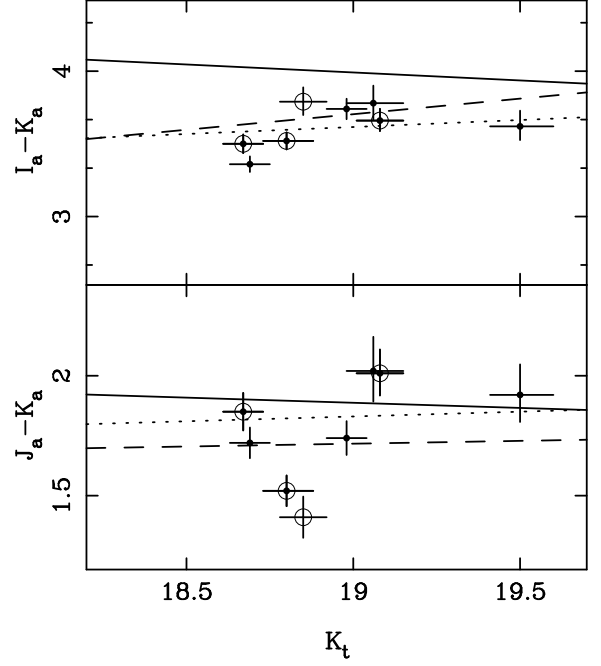


FIG. 24.— Same as Figure 19 but for 3C184 at $z=0.996$.

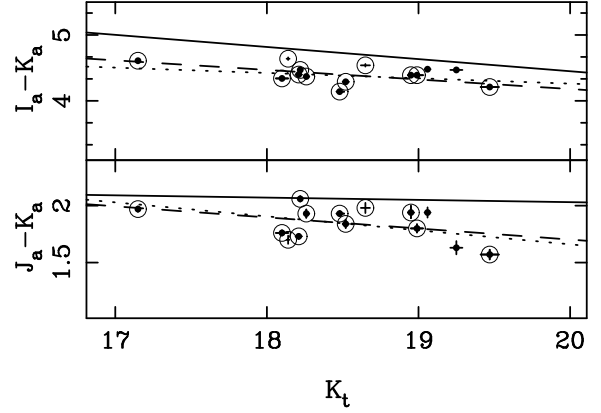


FIG. 25.— Same as Figure 19 but for 3C210 at $z=1.169$. The open circles represent galaxies identified as early-types using GIM2D in the WFPC2 F814W data.

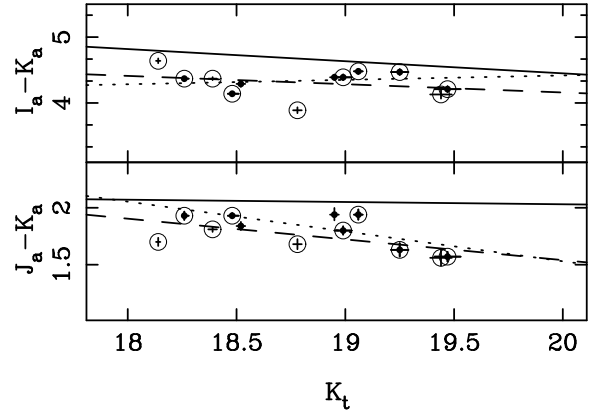


FIG. 26.— Same as Figure 19 but for 3C210 at $z=1.169$. The open circles represent galaxies identified as early-types using GIM2D in the NICMOS F160W data.

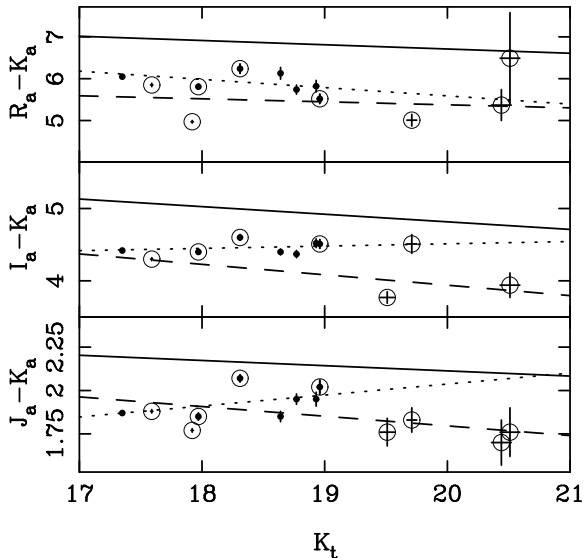


FIG. 27.— Same as Figure 19 but for RDCS 0848+4453 at $z=1.27$. The open circles represent galaxies identified as early-types using GIM2D in the WFPC2 F814W data.

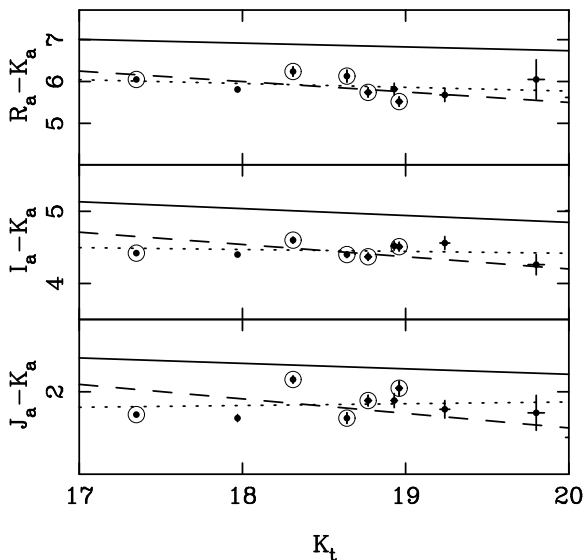


FIG. 28.— Same as Figure 19 but for RDCS 0848+4453 at $z=1.27$. The open circles represent galaxies identified as early-types using GIM2D in the NICMOS F160W data.

ies after we have removed the outliers. We calculated the scatter in the colors from the residuals in the color-magnitude relation after subtracting the predicted Coma slope and the offset from the Coma no-evolution relation we estimated above. However, we change the magnitude limits, as was done in SED98, to $m(L_*)$. We plot the biweight scatter in Figure 31 as was done in SED98. In Figure 32, we plot the biweight scatter around the U-V color-magnitude relation. Strictly speaking, our *blue-red* color is not a true $U - V$, but is created to be as close as possible. For comparison, we plot the Coma result from Bower et al. (1992). Overall, we reaffirm the results of SED98. First, the scatter in the color-magnitude relation has a wavelength dependence, with a larger scatter

as we compare bluer bands with the near-infrared band. The second result is that we measure no change in the scatter with redshift.

5. EVOLUTION IN EARLY-TYPE GALAXY POPULATIONS

In this paper we have extended the range in redshift of the sample of SED98 to $z \simeq 1.3$ and we have doubled the number of clusters of galaxies at $z > 0.8$. Our goals, by extending the range in redshift and number, are to examine the slope and the scatter in the color-magnitude relation to test the ideas of elliptical galaxy formation. By looking at the colors of early-type galaxies, we can only examine the history of the stars, and not the mass assembly. Nonetheless, these photometric properties give us a measure of the average stellar types in the early-type galaxies.

5.1. The Slope of the Color-Magnitude Relation

The slope in the color-magnitude relation is predicted to vary with redshift. In Kauffmann & Charlot (1998), the authors predict a slow change in the slope of the color-magnitude relation, with the relation becoming flat at $z \simeq 1.5$ for cluster early-type galaxies formed by merging smaller mass systems. In contrast, Kodama & Arimoto (1997) predict, for a purely passively evolving stellar population formed at high redshift, that the color-magnitude relation changes only slightly over a wide range in redshift, until very close to the epoch of the formation of the stars in the galaxies. Thus, we are searching for a subtle but important effect: at what redshift does the slope of the color-magnitude relation change? In Figure 29, we find no evidence of a change. We plot the difference between the slope we measure and the slope we measure for the transformed Coma photometry we use as a no-evolution prediction. This is the same plot as Figure 4 in SED98. Shallower slopes, and therefore, flatter color-magnitude relations, appear as positive values in Figure 29.

For some of the clusters, we find a small positive slope difference, implying a general flattening of the color-magnitude relation. In general, none of these results are statistically significant. GHO 0021+0406 shows a strong negative value, and therefore a much steeper slope than expected from the no-evolution result, see Figure 22. We suspect, but cannot prove, that this is from field galaxy contamination as GHO 0021+0406 has a small number of early-type galaxies to begin with. RDCS 0848+4453 was reported to have a flatter than expected slope in van Dokkum et al. (2001), a result we reproduce in Figure 29 for the early-type classification measurement but not when using galaxies identified with GIM2d. In fact, object selection appears to make a significant difference in the measured slopes, as seen by the difference in the slope measurements in Figure 29 for clusters at the same redshift. Such sensitivity implies that, in general, our samples are too small to make reliable slope measurements. We note here that most of the clusters in our sample have on the order of ten or less early-types in the red sequence, while the data in SED98 often had more than twice that number of early-type galaxies. We tried two simple tests to see if any evolution in the slopes existed, a linear fit to the slopes as a function of redshift and power-law evolution as a function of $1 + z$. Neither showed any statistically significant change with redshift. Therefore,

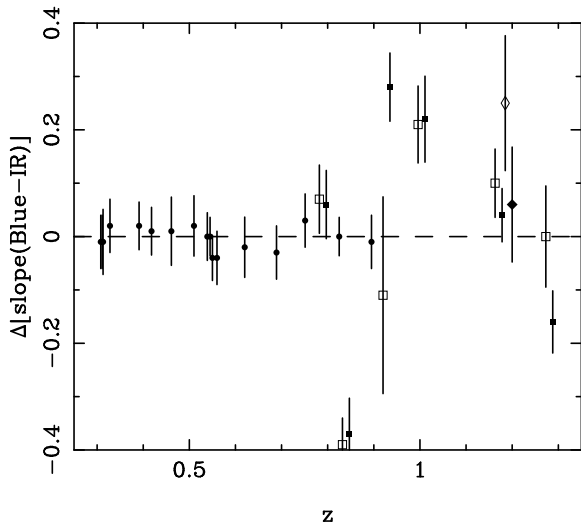


FIG. 29.— The slope of the measured color–magnitude relation minus the slope from the non-evolving Coma relation as a function of redshift for early–type galaxies identified by visual inspection. The solid dots are from SED98. The squares are from this paper with the open squares representing the values from visually classified early–type galaxies and the solid squares representing the results of the automated classification scheme. The solid squares are offset from the cluster redshift for clarity. The diamonds represent the NICMOS results for 3C210 and both the NICMOS and WFPC2 results have been offset slightly in redshift for clarity with open diamond the visual classification result and the solid the automated classification results.

we conclude that we cannot find any evidence of evolution in the slope of the color–magnitude relation but, for us to see such evolution, the trend would have to be much bigger than that predicted in, e.g., Kauffmann & Charlot (1998).

5.2. The Average Color of Early–Type Galaxies

As we have found no measurable evolution in the slope of the color–magnitude relation, we looked for evolution in the offset and in the scatter. The zero-point of the color–magnitude relation must change with time as the stellar populations that make up the cluster early–type galaxies evolve. By measuring the offset as a function of redshift, and assuming a cosmology, we can estimate the average epoch of star formation for the cluster members. This is most easily done by comparing models to no-evolution predictions.

In Figure 30, we plot the predicted color evolution of stellar population synthesis models along with the offsets from the no-evolution Coma color–magnitude relation. As discussed above, these color offsets are measured with respect to a transformed Coma color–magnitude relation. We calculate the theoretical model offsets in two different manners. First, we use the model of de Propris et al. (1999) to describe the colors of an unevolving elliptical galaxy, the same model we use when we compute the relative k-corrections in §4.1. This is a 10 gigayears old single stellar population with solar metallicity and a Salpeter mass function where the stars were formed in a burst of 0.1 gigayears calculated with the 1996 update of Bruzual & Charlot (1993). We subtracted the predicted color of the no evolution model, in the “blue”, “red” and “IR” pass band at the redshift for each cluster, from the

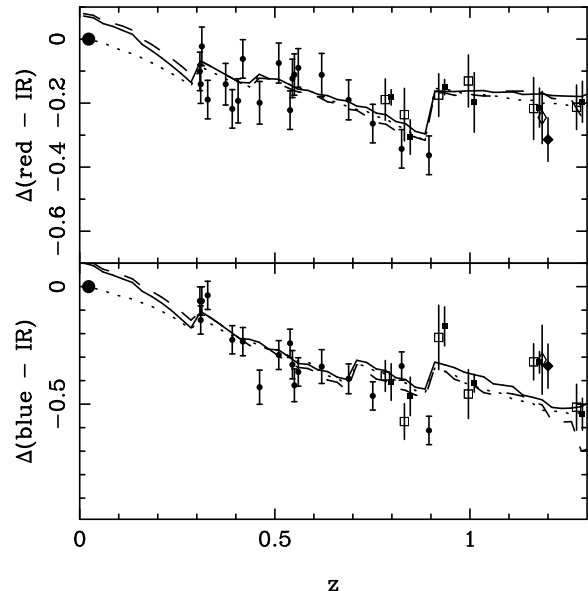


FIG. 30.— The offset from the Coma no-evolution color–magnitude relation as a function of redshift for early–type galaxies identified by visual inspection (open squares) and GIM2D (solid squares). The solid dots are from SED98 and the large solid diamonds represent the value for Coma, fixed to an offset of zero. The diamonds represent the NICMOS results for 3C210 with the open diamond the visually identified early–type galaxies and the solid diamond the GIM2D identified early–type galaxies. The solid lines are Bruzual & Charlot (1996) models for a single stellar population formed with a solar metallicity at a redshift of 5 in an $\Omega = 0.1$ cosmology. The best fitting model using a $\Omega_m = 0.3$, $\Omega_\Lambda = 0.7$ cosmology with the Bruzual & Charlot (1996) models and formation of $z_f = 3$ is the dashed line, while the best fitting Bruzual & Charlot (2003) model, with $z_f = 5$, is the dotted line. All models assume $H_0 = 65 \text{ km s}^{-1} \text{ Mpc}^{-1}$ except for the Bruzual & Charlot (2003) model which assumes $H_0 = 71 \text{ km s}^{-1} \text{ Mpc}^{-1}$, $\Omega_m = 0.27$ and $\Omega_\Lambda = 0.73$.

colors of the evolving models in the same filters at the same redshift. We will refer to this as an absolute measurement. For our second approach, we simply subtract the expected colors of a given model at the redshift of Coma from the expected colors at the redshift of the cluster, which we will call the relative color measure. We try this second approach to test which model best produces the relative change in color as a function of redshift, even if the predicted colors of the model are incorrect. In both cases, we assume that all of the stellar populations making up the early–type galaxies are approximately coeval, that metallicity does not evolve with redshift and that morphological transformations have a minimal effect. We will discuss some of these assumptions further, below.

5.2.1. Older Models and Previous Work

In Figures 30, we plot our data, the offsets, along with the absolute model offsets. First, with a solid line, we plot the best model from SED98 and from Nelson et al. (2001), a single starburst with a formation redshift, $z_f = 5$, and $H_0 = 65 \text{ km s}^{-1} \text{ Mpc}^{-1}$, and $\Omega_m = 0.1$. That model fits the high redshift cluster colors rather well, but predicts colors far too red for the Coma color–magnitude relation. Updating the cosmology to $\Omega_\Lambda = 0.7$ and $\Omega_m = 0.3$ does change the formation

epoch. Using a χ^2 test, we find the best fitting formation epoch from the Bruzual & Charlot (1996) models to be $z_f = 3.0^{+1.8}_{-0.5}$ or that the universe was $2.1^{+0.5}_{-1.0}$ gigayears old when the stars in the galaxies formed. This best fitting model is plotted in Figure 30 as a dashed line. We computed the χ^2 using the difference between the model and both the “blue-IR” and “red-IR” colors. We used errors on the color offset in the divisor but added to that value 0.06 magnitudes of systematic error as described in §4.1. The $\chi^2 = 1.2 - 1.3$ per degree of freedom for these fits are somewhat high, the actual value depending on the classification scheme used for the highest redshift clusters. However, the χ^2 is not so high that we can reject the best fitting model at a high level of significance.

We note here that the $z_f = 3$ model corresponds to the best fitting formation epoch using the evolution of the mass to light ratio from van Dokkum & Stanford (2003). In addition, it is a model in good agreement with the evolution of the K-band luminosity function of de Propris et al. (1999). The work in de Propris et al. (1999) uses the Bruzual & Charlot (1996) stellar population synthesis models as well as the same photometry as this paper, so we have achieved internal consistency for this model comparison.

As found in SED98, however, the colors of the Bruzual & Charlot (1996) model do not match the average color of the Coma cluster members. We find that the best fitting model of SED98 is too red in the “blue-IR” color by 0.09 magnitudes and too red in the “red-IR” by 0.07 magnitudes at the redshift of Coma. The best fitting Bruzual & Charlot (1996) model for the updated cosmology is too red by 0.11 and 0.08 magnitudes in the “blue-IR” and “red-IR” colors respectively. Because of this color mismatch, we also try to compute the relative color evolution of the Bruzual & Charlot (1996) model. We calculate how much the color should have changed at a given redshift as compared with the $z = 0.023$ color. This mimics our actual measurement, where we compare the change in the observed colors with respect to the Coma relation. Here we find no particular formation epoch to be the best fitting. Rather, the χ^2 is flat for very old stellar populations, ones that formed when the universe is 1 gigayear or less in age. This relative evolution test yields different results than the range of allowed formation epochs from the absolute evolution discussed in the previous paragraph. This is because we are not penalizing the models for getting the actual colors wrong, but just seeing which models get the relative change as a function redshift correct. Despite releasing this additional constraint, the model of Bruzual & Charlot (1996) still has a $\chi^2 = 1.3$ per degree of freedom, and $\chi^2 = 1.5$ for the “blue-IR” color, showing that the model does not predict correctly the near ultraviolet color evolution of early-type galaxies.

5.2.2. Bruzual and Charlot 2003 Models

We examined the evolution of the average colors of early-type galaxies in our sample, as well as that in SED98, using the newer Bruzual & Charlot (2003) models. Specifically, we use the Padova 1994 evolutionary tracks, as recommended, with Salpeter initial mass function (Salpeter 1955). These models produce higher formation ages than the Bruzual & Charlot (1996). For example, we find $z_f > 3.0$, or a maximum age of the

universe at the time of formation of 2.9 gigayears, when we use the Bruzual & Charlot (2003) models with solar metallicity and the cosmological values from the Wilkinson Microwave Anisotropy Probe (Bennett et al. 2003) of $\Omega_\Lambda = 0.73$, $\Omega_m = 0.27$ and $H_0 = 71 \text{ km s}^{-1} \text{ Mpc}^{-1}$. The distribution of χ^2 values stays flat to high redshifts as a function of formation age, never crossing the 1σ threshold. There is a shallow minimum at $z_f = 5_{-2.7}$ or an age of $1.6^{+1.3}$ gigayears, but there is no formal upper limit. For this comparison, we only use the relative test mentioned above, where we compare the change of color of the model prediction at a given clusters redshift with respect to the predictions of the same model for the Coma cluster. Given that the Bruzual & Charlot (2003) models do a much better job of reproducing the colors of the Coma cluster, this is effectively the same as the test where we compare with a model chosen to reproduce the colors of Coma early-type galaxies. The relative color evolution therefore only rules out at high significance very recent, $z_f < 1.5$, formation epochs, a result that is true of the Bruzual & Charlot (2003) models because for those models the rate of change in the populations is too fast to match the observed rate of change in the colors for the highest redshift clusters.

Because of the degeneracy between age and metallicity (Worthey 1994, for example), we also compared the change in colors as a function of redshift for both the super-solar ($Z=0.05$) and the $Z=0.008$ sub-solar metallicity populations of Bruzual & Charlot (2003). The super-solar yielded very similar results, namely that $z_f = 5_{-2}$, though the $\chi^2 = 1.77$ per degree of freedom is high enough to reject the high metallicity models at the 99.7%, or three standard deviations, confidence level. Most of the mismatch occurs when comparing the “blue-IR” color offsets. The sub-solar models yielded a minimum $\chi^2 = 15.3$ and, thus are not actually worth discussing. We note here, that we still assume a uniform metallicity for the population of early-type galaxies. Also, in Bruzual & Charlot (2003), the authors mention in Table A1 that the UV and near-infrared colors of their models for super-solar metallicity are “Fair/poor”, which are exactly the colors which we are comparing against. Thus the high apparent significance above could be a reflection of the model’s current uncertainties.

5.2.3. Sources of Uncertainty

It is important for us to note that all of these predictions are based on one set of models, those produced by Bruzual and Charlot, with specific underlying assumptions; a 100 megayears duration starburst, the metal abundance of the stellar population, a Salpeter initial mass function, a flat star formation history and that all of the galaxies in our samples are coeval. As shown in, for example, van Dokkum et al. (1998), changing each of these assumptions can change the formation epoch implied. In Trager et al. (2000), for example, the authors present multiple pieces of evidence that the stellar populations of cluster elliptical galaxies are complicated, with over a factor of two spread in ages and metallicities. Some of this is mitigated by the fact that we are only measuring the pace of the evolution and not trying to actually match the colors of the galaxies with the models directly, hence the mild independence of our results

despite a change in the metallicity of the population. Nonetheless, the spectroscopic techniques of Trager et al. (2000) are far more sensitive to recent bursts of star formation whereas our colors are only measures of the overall average evolution. A complete picture will require a combination of the two approaches to attempt to interpret the history of star formation in early-type galaxies.

In general, the differences between the Bruzual & Charlot (1996) and Bruzual & Charlot (2003) models lie in the treatment of the giant branches and in how the spectral libraries of constituent stars are assembled. One of the key improvements is that while the Bruzual & Charlot (1996) used mostly theoretical models from R. L. Kurucz, Bruzual & Charlot (2003) added empirically more complete stellar models, affecting post main-sequence evolution. The changes in the giant branch stars, which dominate the observed light in the redder bands of early-type galaxies, and the improved stellar libraries, once again for late-type stars which dominate early-type galaxies, explain how the difference between the best fitting models comes about; see Liu et al. (2000) for a more detailed discussion. Given that the colors of early-type galaxies in the Coma cluster are much more closely matched using Bruzual & Charlot (2003), it appears that the later models are a significant improvement over Bruzual & Charlot (1996). Nonetheless, the large change between the two sets of models, in the end, suggests that we only take the most conservative results away from this analysis. Namely, that the average color early-type galaxies evolves as expected for a passively evolving stellar with an average formation epoch definitely with $z_f > 1.5$ and likely with $z_f > 2$, for our adopted cosmology. Interestingly, our results are in excellent agreement with the results of Kelson et al. (2001) who use different models along with very different data to yield the same results. Our formation epoch estimates are, of course, only an average formation epoch. The allowed range of values, and the lower limit, can only be addressed using the scatter of the colors.

5.3. The Scatter in the Color-Magnitude Relation

Our final test for evolution, shown in Figure 32, is the intrinsic scatter around the mean color-magnitude relation. This test was first proposed in Bower et al. (1992). The power of this test is that it is partially model independent. Regardless of when the stars formed, they could not have all formed at the exact same time. As the stellar populations making up the cluster galaxies become older, the scatter in the observed colors becomes less. This relies only on the fact that the time scales for the evolution of a stellar population become longer as the population as a whole becomes older. Using the models from Bruzual & Charlot (1996), we examined what spread in ages would be consistent with the observed spread in colors. For RDCS 0848+4453, for example, the observed biweight scale, or scatter, in the *blue - red* color is 0.06 ± 0.03 , using the visual classifications or 0.04 ± 0.02 from the automated classifications. Using stellar populations models, all with solar metallicity, such a spread in color can be reproduced with a spread in formation times of roughly 1 gigayear, or a spread in the formation epoch from $z_f = 2.5$ to $z_f = 3.8$, assuming a mean formation age of $z_f = 3$, meaning that twice the standard deviation

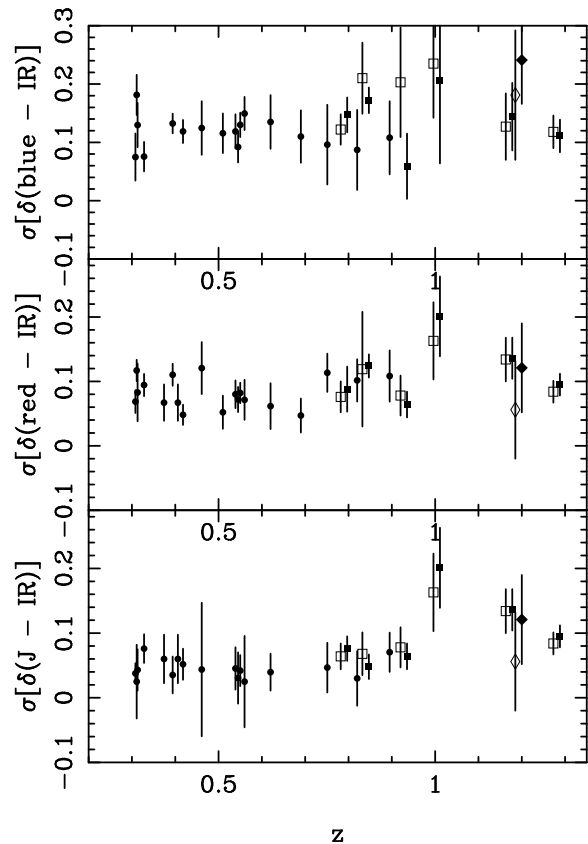


FIG. 31.— The scatter around the color-magnitude relation as a function of redshift. The scatter was calculated for those galaxies identified as early-types. The symbols are the same as in Figures 29 and 30.

in the colors can be contained in that redshift range. The scatter in the *blue - IR* color gives a similar result. Of course, the formation epoch can be pushed to lower redshifts with a corresponding decrease in the spread in formation ages. A mean formation epoch of $z = 2.3$ with a spread in the formation redshift from $z = 2.0$ to $z = 2.5$, roughly 700 megayears, also will reproduce the spread in colors. Given the best fitting formation age of 2.1 gigayears, a spread of 1 gigayear seems reasonable. The rest of the clusters have apparently larger scatters. However, the errors on those scatter measurements are also quite large. For example, in Figure 32, 3C 184 has an apparently large scatter, but the errors are such that it is only two sigma fluctuation from the no-evolution value. This prevents us from translating the observed scatter into a measurement of the scatter in the age to any degree of accuracy. Nonetheless, the other clusters do yield measurements in agreement with the smaller results from RDCS 0848+4453 and from SED98.

Thus, we can create a self-consistent picture. In fact, using the Bruzual & Charlot (2003) models produces the same results. The main possible source of error is in our simple assumptions about the star formation history. We assume above that the distribution of star formation histories matches the distribution of the scatter. However, the results of van Dokkum & Franx (2001) show that we could create other star formation histories, ones where the last stars are formed much closer to the redshift of

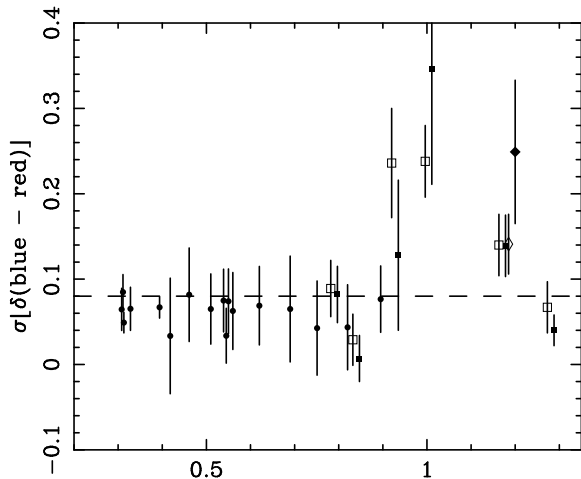


FIG. 32.— The scatter around the color–magnitude relation as a function of redshift for the “blue - red” color. The dashed line is the result from Bower et al. (1992). The symbols are the same as in Figures 29 and 30.

observation and the true spread in ages is much larger than we quote above.

In general, the scatter in the *blue - red* color, as measured in SED98 and in this paper, is statistically consistent with zero, and certainly with the scatter as measured by Bower et al. (1992). We note that, in general, we have only one or two measurements in Figure 31 that are different from the no-evolution value by more than one sigma, results that are entirely consistent with no measured evolution. In a few cases, however, the quality of the photometry is good enough that true scatter has been measured at greater than a 3σ level of confidence. We observe this in the lowest redshift clusters in SED98. For those clusters, the scatter measured is in agreement with Bower et al. (1992). For a couple of the highest clusters, however, we also detect the scatter at $\simeq 3\sigma$ level of confidence. The values we measure are only $\simeq 1-2\sigma$ away from the level as measured by Bower et al. (1992) so we cannot statistically say there is evolution in the scatter. However, evolution in the scatter of the colors of cluster early-type galaxies is expected as observations approach the formation epoch. Given a modest investment in redshifts of cluster members, we should be able to confirm this signal and lower the error on the measured scatter significantly, as has been done for the $z = 1.236$ cluster, RDCS 1252-2927 using the Advanced Camera for Surveys in Blakeslee et al. (2003)

5.4. The Fraction of Early-Type Galaxies

A number of lines of evidence point to a smaller fraction of early-type galaxies at high redshift (Dressler et al. 1997; van Dokkum et al. 2000, 2001), some of the clusters in those samples were included in SED98. In Figure 33 using solid circles, we plot the average fraction of early-type galaxies as a function of redshift. For comparison we plot the average results from Dressler (1980) the results for the Coma cluster from Andreon et al. (1997) and the results from Dressler et al. (1997). At high redshifts, we plot the two cluster early-type fractions for Cl 0023+0423 (GHO 0021+0406 in this

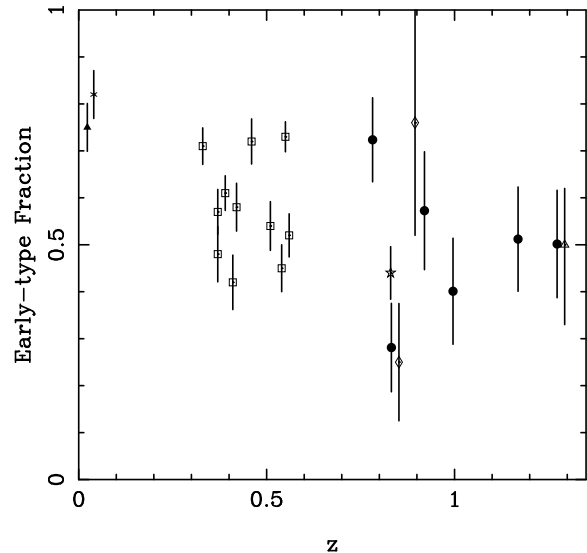


FIG. 33.— The early-type galaxy fraction as a function of redshift. The early-type galaxy fractions for clusters in this paper were measured by counting all of the galaxies that lie within two standard deviations of the the mean color of the early-type galaxies for each cluster and are symbolized by solid circles. At low redshifts, the solid triangle is the value for Coma from Andreon et al. (1997) while the asterisks are the average value from Dressler (1980). The open squares are from Dressler et al. (1997), and the open star is from van Dokkum et al. (2000). The two open diamonds are from Lubin et al. (1998). One of the points is GHO 0021+0406 and is offset from our measurement. Finally, the open triangle is the measurement from RDCS 0848+4453 from van Dokkum et al. (2001).

paper) and Cl 1604+4304 from Lubin et al. (1998), MS 1054-0321 (van Dokkum et al. 2000) and the measurement for RDCS 0848+4453 in van Dokkum et al. (2001).

Our early-type galaxy fraction is calculated in an unusual manner, and thus care should be taken when comparing it with other values. Specifically, we define the fraction as the number of early-type galaxies divided by the total number of galaxies within two standard deviations of the early-type color–magnitude relation and brighter than $m(L_\star) + 0.6$. The magnitude limit was chosen to match van Dokkum et al. (2001), and, therefore, we also reproduce the early-type fraction from that paper in Figure 33. For each cluster, we actually have two measurements of the early-type fraction, one from the automated classification technique and one from visual classification, we then average those two for Figure 33. We perform a weighted average, assuming that each process of morphological identification is independent and, therefore, so are the errors. This method stands in contrast to most measurements which use spectra or colors to pick out cluster members and then measure the early-type galaxy fraction. Nonetheless, our results for clusters with other early-type galaxy fraction measurements are in good agreement. Lubin et al. (1998) finds for GHO 0021+0406 of $25^{+12.5}_{-12.5}\%$ (using the early-type fraction from spectroscopic redshifts, plotted as an open diamond in Figure 33) and van Dokkum et al. (2001) finds for RDCS 0848+4453 an early-type fraction of $50^{+17}_{-12}\%$ (plotted as an open triangle in Figure 33), both of which are close to our average early-type fractions for those

two clusters. Both values from other papers are plotted with an offset in redshift for clarity.

If we ignore the differences between the various methods and simply average the observed early-fractions, we find that in the redshift range of $0.78 < z < 1.273$, excluding the values for GHO 0021+0406, an error weighted early-type fraction of $51 \pm 9\%$. We note here that we quote the weighted value of the error measurements, not the error on the mean, which would be a value of $\pm 6\%$. We exclude GHO 0021+0406 as Lubin et al. (1998) finds that the object is likely to be two groups merging rather than a cluster. Our measured average value is only 3.4σ below the Dressler (1980) value of 82%, thus our results appear strong but are barely statistically significant. Dressler et al. (1997) find an error weighted average value of $60 \pm 4\%$, a more statistically significant result. Taken at face value, we see no evidence for a change in the early-type galaxy fraction from $z \simeq 0.5$ to $z \simeq 1.0$. Potentially there could be mild evolution, in either direction, that we do not see.

As was originally shown in Dressler (1980), there is a relation between early-type galaxy fraction and the density of galaxies. Therefore, a second possible explanation for our lower than expected early-type fractions could simply be that by including all of the galaxies, we are averaging over a lower density than in the lower redshift comparison samples. In addition, many of the objects in our sample are at the low mass end of the range expected from clusters, and, therefore have smaller central galaxy densities.

In §3.4, we discuss our simulations of the automated classification technique. At the magnitude limit imposed for our early-type fraction, we should identify around 70% of the total population of early-type galaxies when using the automated method. Thus, the $z = 0$ value of 80% would be observed as 56% with the addition of 4% of false positive detections. This 60% early-type fraction is within one standard deviation of the observed value of 51%, yielding the possibility that our result could come from misidentification of early-type galaxies at higher redshift as spirals, especially the misidentification of S0 galaxies. Of course, this requires that our misidentification rate for visual classifications matches that for the automated technique. The fact that our overall results agree with other published values also would imply that there is a broad tendency to misclassify galaxies, regardless of the classifier, at high redshift. As we do not have evidence of this, we will simply state that our values represent a lower bound of the true value and that, there is no apparent evolution in the early-type galaxy fraction from $z \simeq 0.5$ to $z \simeq 1.0$.

5.5. Discussion

Our results all indicate that the majority of the stars in the cluster members are formed at $z_f = 2 - 9$, the exact value depending on which particular set of models and results one chooses. As noted before, this is in good agreement with many other studies of luminous cluster early-type galaxies such as in de Propris et al. (1999), van Dokkum & Franx (2001), Nelson et al. (2001) or Kelson et al. (2001). This does yield the puzzling problem of how can the early-type galaxies, that we observe, all have stars that appear to have formed at the same range of high redshifts but the number of early-type

galaxies in the clusters appears to have shrunk at higher redshifts.

The red early-type galaxy members of RDCS 0848+4453 show residual star formation - van Dokkum & Stanford (2003) show spectra of the two brightest galaxies in Figure 28 which have obvious O II emission at 3727\AA . The two brightest members of RDCS 0848+4453 potentially have residual star-formation (or, possibly, a low luminosity AGN but one not detected in X-ray emission, see Stern et al. (2002)), but in general have the typical red colors of high redshift cluster ellipticals, so it would not be surprising to find high redshift cluster ellipticals with even bluer colors, objects that are still forming stars or just recently stopped. We would not include these objects in our sample as we trim out all blue elliptical galaxies before constructing our color-magnitude relation. All of this is discussed as the ‘‘progenitor bias’’ in van Dokkum & Franx (2001). Thus, when we measure the ages of elliptical galaxy star-formation, we are not necessarily measuring the age of formation of stars we see in elliptical galaxies at $z = 0$, but rather the oldest stars at the observed redshifts. The fact that most all methods yield the same epoch of formation, regardless of the redshift range probed, has an interesting consequence. At all redshifts, most clusters seem to be dominated by the light from the oldest stars. It appears that the morphological transformations implied by Figure 33 are both very mild and occur in objects with older stellar populations but not in those objects still forming a majority of their stars at $z = 1 - 2$ as is found in field galaxy surveys. Since linear theory predicts that the most massive objects, namely clusters, should begin to decouple from the Hubble flow first and the smaller dark halos inside these massive objects should collapse early, this is not surprising. The fact that the results of Figure 33 could represent an exaggerated version of the true amount of evolution, if any, only further reinforces this point, namely that there is little late time evolution in the gross properties of the stellar populations of cluster early-type galaxies.

What would be interesting is if the reddest stars in early-type galaxies really did form at $z_f \simeq 5$, as the Bruzual & Charlot (2003) models show. That redshift range is the same as the redshift of the most distant quasars, radio galaxies and the allowed range ends at the appearance of the the Gunn-Peterson trough (Fan et al. 2001; Becker et al. 2001; White et al. 2003). Given those observations point towards a remaining neutral intergalactic medium, a formation redshift $z_f \simeq 5$ is as high as practically can be allowed for the first large number of stars. In addition, given the observed correlation between black hole mass and galaxy bulge mass, luminous quasars must be found in galaxies that have large populations of the old stars found in bulges, the same sorts of stars that make elliptical galaxies. Therefore, we have the intriguing possibility that the oldest stellar populations we find in early-type galaxies could also contain the first significant mass of stars in the history of the universe, the stars that produced most of the first metals - thus populating the intergalactic and intra-cluster medium, and the stars that could have contributed to the re-ionization of the universe. All of this, of course, depends on the assumption of the models of

Bruzual & Charlot (2003), and the assumptions we used in modeling the stellar populations, with the various caveats and problems we have discussed above.

To improve upon our measurements of the evolution of early-type galaxy colors, future samples should be selected with either photometric or spectroscopic redshifts. Field contamination is a difficult problem, as even though with the small areas covered in this sample mean that the expected number of interloping galaxies is small (see our estimates in Table 3), the large scatter on those small numbers of galaxies means that, for any given cluster, there could be a large scatter in the color-magnitude relation. In fact, for many of our high redshift fields, we see such a high scatter—see 3C184 for example. However, a large scatter could also be a natural consequence of finding cluster early-type galaxies close to the epoch of formation. Determining the source of this scatter could greatly increase our understanding of the evolution and formation epoch of early-type cluster galaxies.

A second problem is the additional scatter caused by contamination of the photometry from nearby galaxies. Objects like those shown in Figure 12 are separated in the HST image but are blended together in the lower resolution ground based photometry. This naturally causes an error in the ground based photometry that cannot be removed except in a model dependent manner. However, high resolution observations using, say, the Hubble Space Telescope in multiple bands, remove the need for this.

Future samples of clusters of galaxies will need broad wavelength coverage, stretching from the near-infrared to the rest-frame ultraviolet, and will need high spatial resolution imaging. The natural selection will be a sample of clusters with high virial masses, and therefore a large number of galaxies, and in conjunction with Hubble Space Telescope ACS and NICMOS imaging. Given the evolution of the stars in such a sample, decomposition of the various stellar populations should be possible. Blakeslee et al. (2003) shows the beginnings of one such program. In that work, the authors examine RDCS 1252-2927, at $z = 1.236$, with deep ACS integrations in two bands. Because of the depth of the imaging data, the large number of VLT spectra (31 cluster members to date), and the apparent richness of the cluster, the authors have 31 elliptical galaxies within two standard deviations of the color-magnitude sequence with which to study the same quantities as we do in this paper. That is more early-type galaxies than in the HST imaging of 3C184, 3C210 and RDCS 0848+4453 combined. The high quality of their data means that the slope and scatter are well determined, though the early-type galaxy fractions and the average color evolution cannot be studied with a single cluster. The second necessary component in future studies of early-type galaxies is high resolution, and high signal to noise, spectroscopy to examine the stellar populations. Trager et al. (2000) has shown that, in nearby galaxies, the stellar populations show a great deal of variation in the apparent metal abundance and the age of the episode of the most recent star formation. The combination of tracking the colors, morphological distributions, and the underlying spectral properties of galaxies will give us the opportunity to remove some of the problems that this work has, and, thus, answer the question of when did the stars in early-type galaxies form?

6. SUMMARY

We have constructed a sample of eight clusters of galaxies and galaxy over-densities spanning the redshift range of $0.58 < z < 1.27$ with optical and near-infrared photometry combined with Hubble Space Telescope (HST) morphologies. Of these eight targets, six appear to have a significant red sequence of early-type galaxies. For each cluster, we measure the colors as a function of either K or H band magnitude. The optical bands are all selected to measure a roughly rest-frame U and V band at the redshift of the cluster, so we compare the evolution of the same part of the spectral energy distribution as a function of redshift. The HST imaging data was generally found in the archive, and usually sampled the rest frame B band. In two cases, however, NICMOS data were used that sampled the rest R band.

To morphologically identify galaxies, we chose two approaches. First, we visually classified the galaxies by eye. Second, we used the program GIM2D (Simard et al. 2002) to fit surface brightness profiles. We used a combination of the residuals from the surface brightness profile fit with the bulge to total ratio for an empirically defined measure of the morphological type (Im et al. 2002). For this second approach, we create simulations using images of low redshift galaxies for each observation of a cluster. The simulations used blank sections of the images and the image of the low redshift galaxy from Frei et al. (1996) most closely matching the bandpass of the observations. For most clusters, we found that we could successfully identify 75% of the early-type galaxies at $m(L_*)$ or brighter magnitudes. We also compare our classifications done using the automated classification technique of the Medium Deep Survey (Ratnatunga et al. 1999) and find a good agreement in most cases. For the cluster MS1137.5+6625, we compared our automated classifications with our visual classifications, finding that the two approaches agree 72% of the time, in good agreement with our simulations. In all of the discrepant cases for MS1137.5+6625, objects that were classified as early-type galaxies with our automated technique but as spiral galaxies visually were early spiral galaxies, $T=2$ at the latest, and have colors consistent with the early-type galaxies. The later result means that any resulting bias in the measured statistics of the color-magnitude relation because of the inclusion of spiral galaxies should be small.

For each cluster and galaxy over-density, we constructed color-magnitude relations for the early-type galaxies, creating one sequence for each of the two classification methods. After removing the two over-densities that had too few early-type galaxies to create a red sequence, we measured the slope, scatter and zero-point of the color-magnitude sequences. Regardless of the method for morphological identification we used, the results are similar.

We combined the results in this work with the sample of SED98, or Stanford et al. (1998), to create a sample of 25 measurements of the slope, scatter and average color of cluster early-type galaxies spanning a redshift range of $0.3 < z < 1.3$, all with data acquired in a uniform manner. We measure no apparent evolution in the slope of the color-magnitude relation. However, given the small size of our samples at the highest redshifts

we cannot rule out the evolution as predicted in such work as Kauffmann & Charlot (1998). We examined the shift in the zero-point of the color–magnitude relation, assuming no evolution in the slope of the relation, as a function of redshift. We compare the apparent evolution against the models of Bruzual & Charlot (1993), using the 1996 update, and the models of Bruzual & Charlot (2003). In order to compare our measurement of evolution with other results, we fit for the formation epoch of the stars in the early–type galaxies using coeval starbursts of 0.1 gigayears for a solar metallicity population. We reproduce the work of earlier groups, namely that $z_f = 5$ for a $H_o = 65 \text{ km s}^{-1} \text{ Mpc}^{-1}$, and $\Omega_m = 0.1$ universe and $z_f = 3$ for $\Omega_\Lambda = 0.7$, $\Omega_m = 0.3$ and $H_o = 65 \text{ km s}^{-1} \text{ Mpc}^{-1}$. Updating the models to the Bruzual & Charlot (2003) release and using the WMAP preferred cosmology of $\Omega_\Lambda = 0.73$, $\Omega_m = 0.27$ and $H_o = 71 \text{ km s}^{-1} \text{ Mpc}^{-1}$, we find the average star formation epoch to be $z_f = 5_{-2.7}$ or an age of the universe of $1.6^{+1.3}$ gigayears for early–type galaxies in clusters, regardless of the metallicity of the underlying stellar population. Our measurements of the color scatter agree with other work at these redshifts, such as van Dokkum et al. (2001) and Blakeslee et al. (2003), though many of our clusters have a larger error in the scatter measurements. Using the formalism outlined in van Dokkum & Franx (2001), Blakeslee et al. (2003) finds that the last episodes of significant star-formation occurred at $z_L > 2.7$. If we use the results of van Dokkum & Franx (2001), we find, roughly, $z_L > 3$ for our measurements of the pace of evolution of the average color.

Our results on the epoch of formation depend on the usual assumptions of a coeval population, a single metallicity, and a simple model of star-formation. Results of high-resolution spectroscopy of cluster members, such as in Trager et al. (2000) show that all of these are oversimplifications of the true picture. While we cannot determine how much late time star-formation there would be, we do find that there is, at most, mild, $< 20\%$, evolution in the early–type fraction of cluster galaxies. Thus, if there is a fair amount of late time star-formation, it does not transform the morphologies of the majority of cluster early–type galaxies and it does not grossly change the colors. Rather, we find that cluster early–type galaxies at $z \simeq 1$ are a quiescent population and that the average rest-frame near ultra-violet and blue colors of these galaxies can be described by the process of passive stellar population evolution over the observed range in redshifts.

The authors would like to thank Luc Simard for extensive help in the use of GIM2D. In addition, he provided the modified version of the software we used to fit the multiple NICMOS images. We would also like to thank Myungshim Im for helpful suggestions on classifying early–type galaxies using GIM2D. BH would like to thank Pieter van Dokkum and Marijn Franx for useful discussions on galaxy classification and elliptical galaxy evolution. BH would also like to thank Marc Postman for insights on the morphology-density relation and its impact on early–type galaxy fractions. Finally, we would like to thank the referee, Alfonso Aragón-Salamanca, for many useful suggestions that improved this paper. Support for SAS came from NASA/LTSA grant NAG5-8430 and for BH from NASA/STScI AR7974. Both BH and

SAS are supported by the Institute for Geophysics and Planetary Physics (operated under the auspices of the US Department of Energy by the University of California Lawrence Livermore National Laboratory under contract W-7405-Eng-48). Guest User, Canadian Astronomy Data Centre, which is operated by the Dominion Astrophysical Observatory for the National Research Council of Canada’s Herzberg Institute of Astrophysics.

REFERENCES

- Akritas, M. G. & Bershad, M. A. 1996, *ApJ*, 470, 706
- Andreon, S., Davoust, E., & Heim, T. 1997, *A&A*, 323, 337
- Aragón-Salamanca, A., Ellis, R. S., Couch, W. J., & Carter, D. 1993, *MNRAS*, 262, 764
- Becker, R. H., Fan, X., White, R. L., Strauss, M. A., Narayanan, V. K., Lupton, R. H., Gunn, J. E., Annis, J., Bahcall, N. A., Brinkmann, J., Connolly, A. J., Csabai, I., Czarapata, P. C., Doi, M., Heckman, T. M., Hennessy, G. S., Ivezić, Ž., Knapp, G. R., Lamb, D. Q., McKay, T. A., Munn, J. A., Nash, T., Nichol, R., Pier, J. R., Richards, G. T., Schneider, D. P., Stoughton, C., Szalay, A. S., Thakar, A. R., & York, D. G. 2001, *AJ*, 122, 2850
- Beers, T. C., Flynn, K., & Gebhardt, K. 1990, *AJ*, 100, 32
- Bennett, C. L., Halpern, M., Hinshaw, G., Jarosik, N., Kogut, A., Limon, M., Meyer, S. S., Page, L., Spergel, D. N., Tucker, G. S., Wollack, E., Wright, E. L., Barnes, C., Greason, M. R., Hill, R. S., Komatsu, E., Nolta, M. R., Odegard, N., Peiris, H. V., Verde, L., & Weiland, J. L. 2003, *ApJS*, 148, 1
- Bertin, E. & Arnouts, S. 1996, *A&AS*, 117, 393
- Blakeslee, J. P., Franx, M., Postman, M., Rosati, P., Holden, B. P., Illingworth, G. D., Ford, H. C., Cross, N. J. G., Gronwall, C., Benítez, N., Bouwens, R. J., Broadhurst, T. J., Clampin, M., Demarco, R., Golimowski, D. A., Hartig, G. F., Infante, L., Martel, A. R., Miley, G. K., Menanteau, F., Meurer, G. R., Sirianni, M., & White, R. L. 2003, *ApJ*, 596, L143
- Bower, R. G., Kodama, T., & Terlevich, A. 1998, *MNRAS*, 299, 1193
- Bower, R. G., Lucey, J. R., & Ellis, R. S. 1992, *MNRAS*, 254, 601
- Bruzual, A. G. & Charlot, S. 1993, *ApJ*, 405, 538
- . 1996, personal communication
- Bruzual, G. & Charlot, S. 2003, *MNRAS*, 344, 1000
- Burstein, D. & Heiles, C. 1982, *AJ*, 87, 1165
- Castander, F. J., Ellis, R. S., Frenk, C. S., Dressler, A., & Gunn, J. E. 1994, *ApJ*, 424, L79
- Clowe, D., Luppino, G. A., Kaiser, N., Henry, J. P., & Gioia, I. M. 1998, *ApJ*, 497, L61
- Coleman, G. D., Wu, C.-C., & Weedman, D. W. 1980, *ApJS*, 43, 393
- de Propriis, R., Eisenhardt, P. R., Stanford, S. A., & Dickinson, M. 1998, *ApJ*, 503, L45
- de Propriis, R., Stanford, S. A., Eisenhardt, P. R., Dickinson, M., & Elston, R. 1999, *AJ*, 118, 729
- de Vaucouleurs, G., de Vaucouleurs, A., Corwin, H. G., Buta, R. J., Paturel, G., & Fouque, P. 1991, *Third Reference Catalogue of Bright Galaxies (Volume 1-3, XII, 2069 pp. 7 figs.)*. Springer-Verlag Berlin Heidelberg New York
- Deltorn, J.-M., Le Fevre, O., Crampton, D., & Dickinson, M. 1997, *ApJ*, 483, L21
- Donahue, M., Voit, G. M., Scharf, C. A., Gioia, I. M., Mullis, C. R., Hughes, J. P., & Stocke, J. T. 1999, *ApJ*, 527, 525
- Dressler, A. 1980, *ApJ*, 236, 351
- Dressler, A., Oemler, A. J., Couch, W. J., Smail, I., Ellis, R. S., Barger, A., Butcher, H., Poggianti, B. M., & Sharples, R. M. 1997, *ApJ*, 490, 577
- Eggen, O. J., Lynden-Bell, & Sandage, A. 1962, *ApJ*, 136, 748
- Eisenhardt, P., de Propriis, R., Gonzalez, A., Stanford, S. A., Wang, M., & Dickinson, M. 2004, *ApJ*, in preparation
- Eisenhardt, P., Elston, R., Dickinson, M., Stanford, S. A., & Stern, D. 2001, *ApJS*, in prep
- Ellis, R. S., Smail, I., Dressler, A., Couch, W. J., Oemler, A. J., Butcher, H., & Sharples, R. M. 1997, *ApJ*, 483, 582+
- Faber, S. M. 1973, *ApJ*, 179, 731
- Fan, X., Narayanan, V. K., Lupton, R. H., Strauss, M. A., Knapp, G. R., Becker, R. H., White, R. L., Pentericci, L., Leggett, S. K., Haiman, Z., Gunn, J. E., Ivezić, Ž., Schneider, D. P., Anderson, S. F., Brinkmann, J., Bahcall, N. A., Connolly, A. J., Csabai, I., Doi, M., Fukugita, M., Geballe, T., Grebel, E. K., Harbeck, D., Hennessy, G., Lamb, D. Q., Miknaitis, G., Munn, J. A., Nichol, R., Okamura, S., Pier, J. R., Prada, F., Richards, G. T., Szalay, A., & York, D. G. 2001, *AJ*, 122, 2833
- Freedman, W. L., Madore, B. F., Gibson, B. K., Ferrarese, L., Kelson, D. D., Sakai, S., Mould, J. R., Kennicutt, R. C., Ford, H. C., Graham, J. A., Huchra, J. P., Hughes, S. M. G., Illingworth, G. D., Macri, L. M., & Stetson, P. B. 2001, *ApJ*, 553, 47
- Frei, Z., Guhathakurta, P., Gunn, J. E., & Tyson, J. A. 1996, *AJ*, 111, 174
- Fruchter, A. S. & Hook, R. N. 2002, *PASP*, 114, 144
- Gioia, I. M. & Luppino, G. A. 1994, *ApJS*, 94, 583
- Gioia, I. M., Maccacaro, T., Schild, R. E., Wolter, A., Stocke, J. T., Morris, S. L., & Henry, J. P. 1990, *ApJS*, 72, 567
- Giraud, E. 1998, *AJ*, 116, 1125
- Gunn, J. E., Hoessel, J. G., & Oke, J. B. 1986, *ApJ*, 306, 30
- Henry, J. P., Gioia, I., Maccacaro, T., Morris, S. L., Stocke, J., & Wolter, A. 1992, *ApJ*, 386, 408
- Holtzman, J. A., Burrows, C. J., Casertano, S., Hester, J. J., Trauger, J. T., Watson, A. M., & Worthey, G. 1995, *PASP*, 107, 1065
- Im, M., Simard, L., Faber, S. M., Koo, D. C., Gebhardt, K., Willmer, C. N. A., Phillips, A., Illingworth, G., Vogt, N. P., & Sarajedini, V. L. 2002, *ApJ*, 571, 136
- Kauffmann, G. & Charlot, S. 1998, *MNRAS*, 294, 705
- Kelson, D. D., Illingworth, G. D., Franx, M., & van Dokkum, P. G. 2001, *ApJ*, 552, L17
- Kodama, T. & Arimoto, N. 1997, *A&A*, 320, 41
- Kron, R. G. 1980, *ApJS*, 43, 305
- Liu, M. C., Charlot, S., & Graham, J. R. 2000, *ApJ*, 543, 644
- Lubin, L. M., Postman, M. P., Oke, J. B., Ratnatunga, K. I., Gunn, J. E., Hoessel, J. G., & Schneider, D. P. 1998, *AJ*, 116, 586
- Mathis, J. S. 1990, *ARA&A*, 28, 37
- Nelson, A. E., Gonzalez, A. H., Zaritsky, D., & Dalcanton, J. J. 2001, *ApJ*, 563, 629
- Oke, J. B., Postman, M., & Lubin, L. M. 1998, *AJ*, 116, 549
- Postman, M., Lubin, L. M., & Oke, J. B. 2001, *AJ*, 122, 1125
- Ratnatunga, K. U., Griffiths, R. E., & Ostrander, E. J. 1999, *AJ*, 118, 86
- Rosati, P., Della Ceca, R., Norman, C., & Giacconi, R. 1998, *ApJ*, 492, L21
- Salpeter, E. E. 1955, *ApJ*, 121, 161
- Sandage, A. & Visvanathan, N. 1978, *ApJ*, 225, 742
- Schade, D., Lilly, S. J., Crampton, D., H. F., Le Fevre, O., & Tresse, L. 1995, *ApJ*, 451, 1
- Scodreggio, M. 2001, *AJ*, 121, 2413
- Simard, L., Willmer, C. N. A., Vogt, N. P., Sarajedini, V. L., Phillips, A. C., Weiner, B. J., Koo, D. C., Im, M., Illingworth, G. D. I., & Faber, S. M. 2002, *ApJS*, 142, 1
- Spinrad, H., Marr, J., Aguilar, L., & Djorgovski, S. 1985, *PASP*, 97, 932
- Stanford, S. A., Eisenhardt, P. R., & Dickinson, M. 1998, *ApJ*, 492, 461
- Stanford, S. A., Eisenhardt, P. R., Dickinson, M., Holden, B. P., & De Propriis, R. 2002, *ApJS*, 142, 153
- Stanford, S. A., Eisenhardt, P. R. M., & Dickinson, M. 1995, *ApJ*, 450, 512
- Stanford, S. A., Elston, R., Eisenhardt, P. R., Spinrad, H., Stern, D., & Dey, A. 1997, *AJ*, 114, 2232
- Stanford, S. A., Holden, B., Rosati, P., Tozzi, P., Borgani, S., Eisenhardt, P. R., & Spinrad, H. 2000, *ApJ*, submitted
- Stern, D., Tozzi, P., Stanford, S. A., Rosati, P., Holden, B., Eisenhardt, P., Elston, R., Wu, K. L., Connolly, A., Spinrad, H., Dawson, S., Dey, A., & Chaffee, F. H. 2002, *AJ*, 123, 2223
- Terlevich, A. I., Caldwell, N., & Bower, R. G. 2001, *MNRAS*, 326, 1547
- Trager, S. C., Faber, S. M., Worthey, G., & González, J. J. 2000, *AJ*, 120, 165
- Tully, R. B. & Pierce, M. J. 2000, *ApJ*, 533, 744
- van Dokkum, P. G. & Franx, M. 2001, *ApJ*, 553, 90
- van Dokkum, P. G., Franx, M., Fabricant, D., Illingworth, G. D., & Kelson, D. D. 2000, *ApJ*, 541, 95
- van Dokkum, P. G., Franx, M., Kelson, D. D., & Illingworth, G. D. 1998, *ApJ*, 504, L17+
- van Dokkum, P. G. & Stanford, S. A. 2003, *ApJ*, 585, 78
- van Dokkum, P. G., Stanford, S. A., Holden, B. P., Eisenhardt, P. R., Dickinson, M., & Elston, R. 2001, *ApJ*, 552, L101
- Visvanathan, N. & Sandage, A. 1977, *ApJ*, 216, 214
- White, R. L., Becker, R. H., Fan, X., & Strauss, M. 2003, *AJ*, accepted
- Worthey, G. 1994, *ApJS*, 95, 107

TABLE 1
SUMMARY OF GROUND BASED OBSERVATIONS

Cluster	z	Optical Bands	IR Bands	Aperture	Other Names	Table No. ^a
GHO 0229+0035	0.607	V,I	J,H	1''27	CL 0231+0048	31
GHO 2155+0321	0.7	V,R,I	J,H	1''27	CL 2157+0347	33
MS 1137.5+6625	0.782	R,I	J,H,K	1''50		37
GHO 0021+0406	0.832	R,I	J,H	1''20	CL 0023+0423	39
GHO 1604+4329	0.920	R,I	J,H,K	1''05	CL 1604+4321	42
3C184	0.996	I	J,K	1''50		43
3C210	1.169	I	J,K	1''50		44
RDCS 0848+4453	1.273	B,R,I	J,K	1''20	CL J0848+4453	45

^aRefers to the table in Stanford et al. (2002) where the photometry is tabulated.

TABLE 2
SUMMARY OF HST OBSERVATIONS

Cluster	α^a (J2000)	δ^a (J2000)	Filters	Exposure Time (s)	Table No.
GHO 0229+0035	02:31:43.82	+00:48:47.3	F606W	15300	4
GHO 2155+0321	21:57:52.22	+03:48:06.3	F702W	18800	5
MS 1137.5+6625	11:40:23.86	+66:08:19.4	F814W	14400	6
GHO 0021+0406	00:23:53.76	+04:23:11.1	F702W	17900	7
GHO 1604+4329	16:04:29.45	+43:21:35.4	F702W	19500	8
3C184	07:39:24.28	+70:23:10.8	F814W	11000	9
3C210	08:58:10.58	+27:50:30.0	F814W	26800	10
3C210 1	08:58:09.19	+27:50:47.0	F160W	2624	11
3C210 2	08:58:06.85	+27:51:29.0	F160W	4416	11
3C210 3	08:58:10.98	+27:51:42.0	F160W	5248	11
RDCS 0848+4453	08:48:33.96	+44:53:52.2	F814W	27800	12
RDCS 0848+4453 1	08:48:31.80	+44:53:51.2	F160W	11200	13
RDCS 0848+4453 2	08:48:36.85	+44:53:55.0	F160W	11200	13
RDCS 0848+4453 3	08:48:34.72	+44:53:08.0	F160W	11200	13

^aCenter of HST pointing or first image in dither pattern

TABLE 3
SUMMARY OF MERGED CATALOGS

Cluster	z	$m(L_*)^a$	$N < m(L_*)$	$N_{early} < m(L_*)^b$	$N_{e,pred} < m(L_*)$
GHO 0229+0035	0.607	18.7 (18.9) ^c	12	4/3	1.4
GHO 2155+0321	0.7	19.2 (19.4) ^c	19	3/2	2.1
MS 1137.5+6625	0.782	18.6 (18.8)	23	15/16	2.6
GHO 0021+0406	0.832	19.7 (19.8) ^c	18	4/3	1.3
GHO 1604+4329	0.920	19.0 (19.1)	30	10/11	1.9
3C184	0.996	19.2 (19.3)	23	10/6	2.5
3C210	1.169	19.6 (19.7)	33	11/15	1.6
RDCS 0848+4453	1.273	19.9 (20.0)	27	10/8	2.4

^aNon-evolving value of $m(L_*)$ for $\Omega_m = 0.1$, $\Omega_\Lambda = 0.0$ and for $\Omega_m = 0.3$, $\Omega_\Lambda = 0.7$ in parentheses. Both values use $H_0 = 65 \text{ km s}^{-1} \text{ Mpc}^{-1}$

^bTwo numbers of early-type galaxies are given. The first is the number identified visually, the second is the number identified automatically

^cValue of $m(L_*)$ in H band for these clusters, not K as in SED98.

TABLE 4
GHO 0229+0035 HST IMAGING DATA

ID	δx (")	δy (")	T Type	B/T	Res.	R_h (")	Chip	Pos.
2	-23.9	-32.3	-10	0.00	-199.98	0.048	wf3	(557, 298)
3	0.0	0.0	-10	0.54	-199.98	0.011	wf2	(36, 351)
4	-80.5	81.3	5	0.00	0.15	1.784	wf4	(361, 692)
5	19.4	24.6	4	0.01	0.22	0.572	wf2	(318, 210)
6	-71.1	22.0	-1	0.97	0.03	0.637	wf4	(510, 111)
7	8.0	20.0	-2	0.56	0.21	0.470	wf2	(191, 203)
8	50.0	63.0	4	0.11	0.17	0.847	wf3	(705, 408)
9	-37.3	25.1	5	0.00	0.21	1.269	wf4	(190, 15)
11	-56.9	27.3	3	0.42	0.15	0.390	wf4	(359, 100)
12	17.3	-8.4	-1	0.89	0.02	0.208	wf2	(151, 505)
13	-31.0	10.5	-3	0.29	0.01	0.389	wf3	(131, 186)
16	30.6	25.9	2	0.71	0.31	0.306	wf2	(420, 246)
17	-66.5	42.0	3	0.02	0.21	0.629	wf4	(394, 270)
18	-44.5	72.7	4	0.04	0.17	1.151	wf4	(64, 467)
19	-40.0	11.0	0	0.28	0.08	0.305	wf3	(93, 266)
20	-43.5	27.2	7	0.00	0.22	0.841	wf4	(240, 46)
22	-33.1	-7.2	3	0.17	0.09	0.696	wf3	(290, 279)
23	-63.9	88.0	8	0.03	0.02	0.913	wf4	(181, 688)
24	-41.9	-13.9	-4	0.11	0.03	0.009	wf3	(316, 380)
25	-51.0	58.2	8	0.72	0.10	0.708	wf4	(177, 354)
26	-49.2	-5.0	8	0.13	0.12	0.321	wf3	(206, 407)
27	-63.3	71.2	8	0.13	0.10	0.815	wf4	(231, 534)
28	10.8	36.4	6	0.05	0.12	1.053	wf2	(288, 67)
29	-48.3	-23.8	5	0.07	0.10	0.949	wf3	(378, 482)
30	-58.6	36.7	6	0.00	0.23	1.287	wf4	(332, 195)
31	-78.8	29.6	4	0.23	0.08	0.554	wf4	(550, 211)
32	-86.1	12.0	-5	0.00	0.06	0.034	wf4	(689, 82)
33	2.7	-27.0	-3	0.79	0.09	0.212	wf3	(620, 30)
36	40.3	-10.1	5	0.35	0.00	0.159	wf2	(361, 608)
37	-82.6	68.9	-10	0.30	-199.98	0.017	wf4	(429, 585)
39	-74.5	56.0	2	0.07	0.12	0.691	wf4	(403, 435)
40	-52.6	30.6	1	0.67	0.00	0.214	wf4	(304, 113)
41	15.2	-1.0	8	0.03	0.11	0.631	wf2	(177, 424)
42	-6.6	-38.9	0	0.32	0.13	0.016	wf3	(693, 162)
43	7.5	38.2	1	0.00	0.09	0.234	wf2	(262, 36)
45	-22.0	-0.8	-7	0.81	0.03	0.211	wf3	(263, 155)
46	-9.0	21.3	1	0.49	0.03	0.113	wf2	(42, 120)
47	22.6	47.7	0	0.37	0.06	0.150	wf2	(434, 15)
48	-63.6	21.1	2	0.36	-0.03	0.399	wf4	(445, 65)

TABLE 5
GHO 2155+0321 HST IMAGING DATA

ID	δ_x (")	δ_y (")	T Type	B/T	Res.	R_h (")	Chip	Pos.
1	-65.7	58.8	-10	0.40	0.64	0.557	wf2	(303, 239)
2	-47.0	62.7	-10	0.00	-199.98	0.558	wf2	(117, 293)
3	18.0	-38.7	-10	0.43	0.15	0.147	wf4	(612, 639)
7	36.3	81.0	-3	0.93	0.04	0.765	wf3	(549, 677)
8*	0.0	0.0	5	0.00	0.20	1.368	wf4	(392, 275)
8*	0.0	0.0	-10	0.24	-0.13	1.65	wf4	(394, 264)
9	-18.3	37.1	-10	0.06	-199.98	0.115	wf3	(66, 172)
11	-48.7	82.3	-1	0.40	0.02	0.744	wf2	(156, 483)
14	-3.7	49.3	-1	0.48	0.05	0.440	wf3	(197, 305)
18	-18.5	-0.6	-9	0.03	-0.17	2.715	wf4	(212, 289)
24	20.1	-0.9	-9	0.40	0.01	0.011	wf4	(593, 257)
26	3.2	50.2	-8	0.00	0.34	0.500	wf3	(212, 372)
31	-13.1	85.1	-6	0.00	0.04	0.018	wf3	(547, 180)
34	2.2	35.7	0	0.14	0.03	0.505	wf3	(69, 376)
36	-1.1	-17.7	4	0.33	0.18	1.17	wf4	(400, 443)
37	22.2	92.1	2	0.47	0.16	0.552	wf3	(649, 529)
39	4.2	59.0	-10	0.03	-199.98	0.025	wf3	(301, 377)
40	17.3	15.3	8	0.00	0.10	0.829	wf4	(558, 99)
41	-42.6	66.2	3	0.41	0.32	1.622	wf2	(79, 328)
42	8.1	-3.4	1	0.00	0.07	0.370	wf4	(476, 292)
43*	-14.8	71.9	1	0.00	0.14	0.455	wf3	(429, 188)
43*	-14.8	71.9	7	0.00	0.13	0.907	wf3	(408, 171)
47	-27.3	22.9	1	0.02	0.10	0.420	wf4	(103, 64)
48	-21.4	56.2	-2	0.55	0.05	0.121	wf3	(252, 125)
49	-25.2	53.7	2	0.07	0.07	0.391	wf3	(223, 90)
52	-5.3	16.5	5	0.01	0.22	0.999	wf4	(327, 107)
53	31.8	33.2	0	0.98	0.08	0.012	wf3	(69, 673)
54	-18.1	76.7	-3	0.56	0.08	0.011	wf3	(458, 142)
55	-17.8	94.3	-8	0.03	0.16	2.476	wf3	(638, 127)
58	14.7	29.3	9	0.19	0.23	0.855	wf3	(17, 502)
62	25.2	-41.5	-2	0.77	0.01	0.009	wf4	(685, 658)
65	29.9	77.3	-8	0.00	-199.98	0.034	wf3	(508, 617)
66	-12.3	45.9	-8	0.06	0.07	0.752	wf3	(160, 229)

TABLE 6
MS 1137.5+6625

ID	δ_x (")	δ_y (")	T Type	B/T	Res.	R_h (")	Chip	Pos.
3	0.0	0.0	-5	0.68	0.04	2.649	wf3	(492, 314)
8	4.4	9.7	-5	0.78	0.07	0.616	wf3	(455, 412)
10	2.2	3.3	-5	0.66	0.04	0.720	wf3	(471, 348)
11	7.4	-6.8	-2	0.64	0.12	0.070	wf3	(415, 252)
12	8.3	-5.0	-3	0.88	0.06	0.401	wf3	(411, 273)
13	-11.3	12.5	-4	0.24	0.11	0.442	wf3	(612, 429)
14	26.1	14.7	-10	0.00	0.22	0.035	wf3	(245, 476)
15	-1.1	4.9	-2	0.99	0.04	0.553	wf3	(508, 362)
17	3.8	2.4	-1	0.82	0.06	0.422	wf3	(456, 338)
20	-4.9	6.2	-2	0.41	0.02	0.649	wf3	(546, 370)
21	5.9	6.1	-4	0.95	0.03	0.349	wf3	(438, 378)
23	37.7	33.7	-1	0.36	0.07	0.754	wf3	(143, 673)
24	2.2	38.1	-5	0.77	0.02	0.302	wf3	(494, 692)
25	-26.6	9.1	2	0.61	0.07	0.825	wf4	(283, 314)
27	-11.2	-25.2	4	0.36	0.14	1.289	wf3	(589, 56)
28	41.4	31.7	-3	0.51	0.08	0.321	wf3	(101, 655)
29	29.8	-3.9	-1	0.64	0.08	0.834	wf3	(194, 289)
30	43.0	-13.2	-3	0.98	0.02	0.361	wf3	(57, 209)
31	6.5	-3.0	-2	0.99	0.04	0.511	wf3	(427, 288)
32	7.9	9.4	1	0.68	0.07	0.053	wf3	(420, 411)
34	-1.4	-2.0	-4	0.78	0.09	0.352	wf3	(505, 291)
39	-10.8	-10.4	0	0.72	0.03	0.273	wf3	(595, 204)
40	12.3	-49.6	-1	0.74	0.11	0.539	wf2	(156, 332)
41	44.7	3.5	0	0.88	0.07	0.37	wf3	(50, 375)
47	21.1	-45.2	5	0.01	0.18	1.018	wf2	(107, 247)
49	32.1	7.9	-3	0.62	0.06	0.229	wf3	(179, 412)
50	12.4	-5.9	2	0.27	0.07	0.379	wf3	(364, 262)
54	2.0	-11.1	-3	0.64	0.03	0.289	wf3	(466, 205)
55	29.1	36.2	5	0.03	0.12	0.735	wf3	(225, 690)
56	-5.3	11.4	1	0.84	0.05	0.204	wf3	(553, 422)
57	29.7	-6.5	-1	0.67	0.07	0.246	wf3	(194, 270)
58	71.7	-16.0	7	0.23	0.13	0.333	wf4	(208, 207)
59	-22.4	-64.7	3	0.51	0.29	0.199	wf2	(330, 670)
60	18.5	31.5	1	0.20	0.13	0.333	wf3	(330, 638)
61	-22.9	-50.6	-3	0.81	0.09	0.290	wf2	(183, 684)
62	-7.1	-11.5	-3	0.84	0.01	0.234	wf3	(556, 195)
65	13.8	-19.5	2	0.00	0.08	0.488	wf3	(343, 129)
71	-11.1	15.6	-4	0.80	0.03	0.202	wf3	(612, 460)
72	15.6	-13.3	0	0.73	0.04	0.542	wf3	(330, 191)
73	41.5	-25.5	-4	0.50	0.05	0.158	wf3	(63, 83)
75	-2.9	-27.6	5	0.00	0.26	0.695	wf3	(504, 38)
78	66.5	14.7	2	0.39	0.03	0.292	wf4	(510, 142)
81	30.7	28.4	-2	0.64	0.07	0.211	wf3	(207, 616)
82	0.8	-39.9	1	0.88	-0.02	0.403	wf2	(67, 452)
83	17.1	-7.8	1	0.32	0.16	0.335	wf3	(320, 246)
84	-2.2	-21.1	2	0.00	0.72	0.034	wf3	(501, 103)
85	13.8	-10.2	6	0.57	0.21	1.160	wf3	(345, 224)
88	-24.8	1.1	-3	0.85	-0.04	0.430	wf3	(740, 309)
90	-11.9	-43.9	-1	0.48	0.12	0.300	wf2	(115, 571)
91	6.7	-30.0	-3	0.60	0.07	0.441	wf3	(405, 20)
93	5.4	-35.2	1	0.76	0.02	0.215	wf2	(13, 410)
95	14.3	11.9	7	0.47	0.23	0.537	wf3	(360, 440)
96	-7.6	23.4	9	0.03	0.12	1.601	wf3	(580, 540)
98	15.3	35.8	-3	0.28	0.28	0.029	wf3	(363, 677)
102	43.0	-17.1	-10	0.11	0.28	0.468	wf3	(50, 169)
103	5.6	20.8	-1	0.48	0.07	0.201	wf3	(453, 522)
107	-12.9	-3.3	-3	0.97	0.04	0.099	wf3	(616, 274)
110	39.4	-20.9	-2	0.70	0.10	0.194	wf3	(86, 132)
112	68.4	-30.9	0	0.01	0.10	0.239	wf4	(55, 190)
114	13.6	-63.6	-1	0.73	0.06	0.212	wf2	(298, 308)
115	39.3	-55.9	3	0.36	0.09	0.614	wf2	(202, 53)
116	23.0	1.4	2	0.16	0.02	0.842	wf3	(265, 343)
118	22.3	-0.3	-2	0.68	0.02	0.253	wf3	(273, 324)
119	19.0	-7.6	-3	0.70	0.04	0.190	wf3	(301, 249)
121	-4.1	25.0	5	0.01	0.14	0.827	wf3	(550, 558)
123	26.7	-42.6	2	0.76	0.05	0.360	wf2	(77, 192)
125	-17.0	10.2	1	0.28	0.05	0.157	wf3	(669, 404)
126	13.1	-40.9	6	0.00	0.10	0.786	wf3	(335, 66)
128	14.2	-25.7	-2	0.00	0.13	0.298	wf2	(67, 331)
129	-14.6	-49.2	9	0.00	0.15	0.699	wf2	(171, 601)
133	-10.3	27.7	-7	0.18	0.21	0.050	wf3	(611, 585)

TABLE 7
GHO 0021+0406 HST IMAGING DATA

ID	δ_x (")	δ_y (")	T Type	B/T	Res.	R_h (")	Chip	Pos.
10	-65.6	-39.4	5	0.18	0.23	0.725	wf3	(493, 475)
11	-25.4	-56.1	7	0.00	0.26	1.123	wf3	(590, 49)
12	-25.9	-2.5	-3	0.49	0.02	0.573	wf3	(58, 142)
17	-8.1	12.5	8	-1	-1	-1	wf4	(4, 98)
18	11.1	-26.0	8	0.99	0.20	0.627	wf2	(245, 229)
19	0.9	-42.4	-1	0.60	0.05	0.217	wf2	(166, 399)
20	18.3	-45.5	5	0.08	0.19	1.076	wf2	(345, 408)
21	-51.9	-10.0	10	0.06	0.17	0.838	wf3	(174, 385)
22	-37.9	-57.8	10	0.10	0.18	0.804	wf3	(628, 170)
23	-69.8	1.8	0	0.41	0.09	0.287	wf3	(88, 583)
24	-54.3	18.6	4	0.12	0.08	1.148	wf4	(477, 63)
25	51.9	-65.3	6	0.04	0.00	1.259	wf2	(725, 560)
26	-19.1	68.2	6	0.51	0.09	1.184	wf4	(206, 629)
29	-8.7	-6.2	-3	0.48	0.01	0.267	wf2	(16, 58)
31	-33.9	0.4	1	0.01	0.06	0.662	wf3	(36, 231)
32	-76.4	-10.1	7	0.00	0.09	0.207	wf3	(222, 626)
33	2.2	-33.4	10	0.01	0.15	0.763	wf2	(168, 310)
34	-19.8	15.4	0	0.42	0.03	0.211	wf4	(120, 109)
37	-62.1	-24.9	-5	0.00	0.09	0.007	wf3	(342, 463)
39	-66.0	-60.0	0	0.06	0.15	0.417	wf3	(701, 447)
40	-54.1	-0.4	8	0.01	0.13	0.591	wf3	(85, 421)
43	54.0	-13.7	1	0.62	-0.01	0.872	wf2	(651, 32)
46	40.7	-48.6	4	0.21	0.19	0.415	wf2	(574, 404)
49	51.6	-47.3	6	0.06	0.01	0.497	wf2	(681, 374)
50	-64.4	3.4	10	0.02	0.18	0.426	wf3	(66, 530)
52	-22.1	-55.9	9	0.08	0.20	0.875	wf3	(580, 16)
53	-39.8	38.2	0	0.37	0.16	0.281	wf4	(358, 297)
54	-70.5	-15.8	1	0.14	0.08	0.416	wf3	(265, 562)
55	8.8	-30.4	2	0.10	0.08	0.484	wf2	(221, 270)
56	34.0	-57.3	-2	0.28	0.19	0.218	wf2	(523, 498)
57	12.2	-29.5	-5	1.00	0.02	0.006	wf2	(261, 257)
60	42.7	-66.1	-4	0.85	0.04	0.137	wf2	(626, 577)
61	-32.8	-9.3	-4	0.39	0.08	0.304	wf3	(137, 197)
62	14.8	-59.3	4	0.27	0.15	0.832	wf2	(334, 551)
63	-65.5	17.3	-1	0.02	0.13	0.202	wf4	(575, 45)
65	-23.4	17.7	1	0.60	0.20	0.292	wf4	(161, 125)
73	-68.9	-4.8	-1	0.02	0.03	0.301	wf3	(154, 565)
74	-28.1	-49.4	10	0.03	0.09	0.820	wf3	(527, 83)
79	-17.9	-5.3	8	0.01	0.08	0.383	wf3	(72, 56)
80	5.1	-14.9	10	0.36	0.06	0.523	wf2	(171, 124)
82	-19.3	29.6	3	0.01	0.23	0.615	wf4	(140, 247)
86	-8.2	25.7	9	0.11	0.05	0.541	wf4	(22, 230)
87	-46.8	55.9	8	0.01	0.16	0.757	wf4	(457, 459)
88	-12.3	-24.7	-3	-1	-1	-1	wf2	(5, 219)
89	-53.7	40.9	-4	0.75	0.00	0.015	wf4	(499, 300)
91	-19.0	-16.2	1	0.09	0.16	0.453	wf3	(178, 49)

TABLE 8
GHO 1604+4329 HST IMAGING DATA

ID	δ_x (")	δ_y (")	T Type	B/T	Res.	R_h (")	Chip	Pos.
3	-33.8	47.4	-10	0.00	-199.98	0.609	wf2	(258, 312)
5	-80.7	-7.0	-10	0.00	-199.98	0.578	wf3	(192, 426)
6	12.6	64.1	4	0.14	0.15	1.188	wf2	(641, 633)
7	-18.7	46.7	-1	0.43	0.03	0.752	wf2	(330, 448)
10	-37.9	11.2	-4	0.18	0.05	0.337	wf3	(465, 49)
13	-21.4	1.5	1	0.63	0.04	0.621	wf3	(655, 52)
14	7.7	35.0	-3	0.59	0.07	0.073	wf2	(363, 734)
17	-15.0	0.7	1	0.63	0.07	1.043	wf3	(712, 29)
18	-87.7	-38.6	5	0.23	0.07	1.393	wf3	(289, 727)
20	-24.9	-3.8	-2	0.71	0.04	0.364	wf3	(652, 113)
21	-21.8	29.9	0	0.73	0.06	0.405	wf2	(171, 502)
22	-54.5	19.9	3	0.03	0.19	1.577	wf3	(280, 58)
23	-1.3	51.2	9	0.37	0.27	0.554	wf2	(458, 574)
27	-19.1	48.0	4	0.01	0.17	0.740	wf2	(342, 437)
28	-46.2	-18.5	-9	0.46	0.01	0.276	wf3	(540, 347)
30	-8.6	31.5	-3	0.82	0.05	0.406	wf2	(251, 611)
31	-32.3	-4.3	1	0.29	0.06	0.510	wf3	(591, 156)
32	6.7	43.9	-3	0.47	0.02	0.267	wf2	(433, 681)
35	-31.9	63.3	3	0.00	0.17	0.575	wf2	(411, 251)
36	-39.9	85.1	-1	0.02	0.08	0.367	wf2	(558, 74)
39	-41.5	-19.7	-3	0.78	0.03	0.699	wf3	(588, 333)
40	-53.0	-41.1	4	0.07	0.06	0.690	wf3	(597, 578)
42	-28.3	31.7	-1	0.44	0.00	0.196	wf2	(155, 437)
43 ^a	-78.8	-9.5	-2	0.67	0.84	1.156	wf3	(216, 434)
45	-26.5	-15.1	7	0.00	0.26	0.496	wf3	(697, 220)
50	-47.2	43.1	1	0.84	0.02	0.315	wf2	(161, 220)
52	-93.0	-5.8	6	0.00	0.15	0.669	wf3	(75, 477)
53	-44.4	-22.6	1	0.26	0.02	0.316	wf3	(577, 373)
54	-32.4	71.6	5	0.04	0.24	0.945	wf2	(480, 206)
58	2.7	45.1	2	0.66	-0.01	0.287	wf2	(423, 642)
62	-38.9	74.1	-3	0.85	0.02	0.187	wf2	(470, 136)
65	-26.8	14.7	1	0.45	0.15	0.573	wf2	(17, 539)
70	-43.9	-41.7	8	0.00	0.17	0.444	wf3	(679, 537)
71	-21.1	77.1	1	0.82	0.04	0.225	wf2	(583, 274)
73	-55.6	43.4	7	0.01	0.16	0.69	wf2	(124, 145)
78	-22.6	81.3	-1	0.67	0.16	0.426	wf2	(612, 241)
79	-25.4	4.2	2	0.38	0.16	0.659	wf3	(607, 48)
80	-8.4	83.9	-6	0.87	-0.12	0.162	wf2	(708, 351)
85	-10.8	10.8	3	0.36	0.09	0.666	wf2	(60, 691)
88	-18.8	68.1	2	0.08	0.05	0.356	wf2	(515, 345)
90	0.8	33.2	1	0.01	0.09	0.303	wf2	(315, 684)
91	-1.9	19.8	0	0.61	0.02	0.128	wf2	(180, 728)
94	-40.6	-24.7	4	0.00	0.21	0.438	wf3	(620, 372)

^aThis object is next to the bright star, object # 5. The GIM2D parameters were affected by the strongly varying background.

TABLE 9
3C184 HST IMAGING DATA

ID	δx ($''$)	δy ($''$)	T Type	B/T	Res.	R_h ($''$)	Chip	Pos.
1	19.5	16.3	2	0.70	0.07	0.917	wf3	(645, 429)
2	8.4	4.9	3	0.02	0.12	1.531	wf3	(487, 398)
3	0.0	0.0	7	0.57	0.27	0.861	wf3	(399, 355)
4	-30.2	-13.1	-3	0.94	0.02	0.528	wf3	(120, 172)
5	-30.8	-20.6	4	0.06	0.12	1.032	wf3	(51, 209)
6	-52.7	-45.8	5	0.30	0.19	1.516	wf4	(174, 268)
7	-25.3	51.6	-2	0.94	0.04	0.014	wf2	(126, 688)
8	21.6	1.1	-1	0.58	0.04	0.385	wf3	(529, 530)
9	-81.7	67.4	1	0.06	0.10	0.579	wf2	(701, 516)
10	15.2	27.3	3	0.07	0.15	0.737	wf3	(714, 332)
11	-81.2	15.3	0	0.03	0.10	0.608	wf2	(403, 71)
12	2.4	2.1	-3	0.74	-0.01	0.419	wf3	(431, 365)
13	19.5	-20.4	7	0.03	0.15	0.795	wf3	(333, 633)
14	-42.1	48.0	4	0.49	0.13	0.723	wf2	(248, 566)
15	-38.4	-68.8	-2	0.97	0.00	0.255	wf4	(422, 382)
16	15.4	-20.9	3	0.02	0.10	0.567	wf3	(293, 601)
17	-85.3	-68.1	-1	0.01	0.05	0.035	wf4	(20, 649)
18	7.9	20.1	-3	0.86	-0.01	0.298	wf3	(614, 309)
19	12.9	19.0	-2	0.80	0.03	0.127	wf3	(630, 357)
20	3.9	7.0	-2	0.19	0.01	0.250	wf3	(481, 346)
21	-1.1	-24.5	8	0.03	0.07	0.958	wf3	(187, 482)
22	-63.3	-41.3	-1	0.34	0.02	0.268	wf4	(58, 290)
23	-58.9	-48.2	8	0.01	0.23	0.997	wf4	(132, 318)
24	-4.7	7.0	-2	0.57	0.02	0.180	wf3	(431, 277)
25	38.1	12.5	0	0.68	0.02	0.286	wf3	(717, 611)
26	15.1	-4.4	1	0.01	0.15	0.248	wf3	(444, 505)
27	-52.5	41.4	-1	0.20	0.11	0.375	wf2	(300, 448)
28	-2.1	10.4	-2	0.22	-0.03	0.163	wf3	(472, 280)
29	10.5	-9.7	-7	1.00	0.01	0.011	wf3	(374, 496)
30	-18.4	-8.3	7	0.08	0.20	0.736	wf3	(226, 249)
31	-51.4	33.7	0	0.31	0.16	0.166	wf2	(252, 392)
32	-83.5	71.8	9	0.05	0.09	0.651	wf2	(727, 544)
33	-2.9	-67.0	8	0.00	0.09	0.669	wf4	(718, 168)
34	-48.9	-40.7	1	0.34	0.02	0.447	wf4	(177, 201)
35	-2.6	12.4	7	0.07	-0.07	0.772	wf3	(489, 266)

TABLE 10
3C210 HST WFPC2 IMAGING DATA

ID	δ_x ($''$)	δ_y ($''$)	Class ^a	B/T	Res.	R_h ($''$)	Chip	Pos.
2	21.7	36.7	1	0.44	0.06	0.490	wf4	(42, 65)
3	0.0	0.0	4	0.23	0.15	0.898	wf2	(123, 301)
4	-6.5	27.8	4	0.31	0.16	0.467	wf3	(199, 125)
5	32.6	-41.0	3	0.01	0.23	1.486	wf2	(648, 277)
6	23.2	-31.1	1	0.59	0.06	0.522	wf2	(511, 294)
7	28.8	-19.8	5	0.00	0.23	0.115	wf2	(451, 181)
8	-11.6	12.7	1	0.19	0.03	0.361	wf3	(325, 34)
9	-21.4	7.3	1	0.63	0.04	0.552	wf3	(438, 45)
10	21.8	54.8	2	0.03	0.07	0.661	wf4	(191, 170)
11	-44.8	6.5	2	0.06	0.08	0.609	wf3	(634, 173)
12	25.8	46.6	1	0.01	0.06	0.300	wf4	(99, 157)
13	25.8	-50.9	1	0.70	0.04	0.295	wf2	(689, 390)
14	-16.5	15.8	2	0.66	0.03	0.205	wf3	(350, 86)
15	6.4	-26.1	1	0.62	0.06	0.666	wf2	(370, 401)
16	-17.5	55.4	1	0.45	0.04	0.637	wf3	(128, 413)
17	-8.0	13.6	1	0.86	0.02	0.371	wf3	(292, 18)
18	43.2	-15.0	3	0.19	0.21	1.204	wf2	(500, 37)
19	-37.5	14.3	4	0.12	0.08	0.590	wf3	(528, 195)
20	-11.0	24.6	4	0.01	0.24	0.308	wf3	(250, 125)
21	-2.5	-6.7	2	0.37	-0.01	0.415	wf2	(82, 360)
22	-3.8	9.5	1	0.03	0.09	0.257	wf2	(21, 275)
23	2.5	10.1	4	0.00	0.27	0.714	wf2	(53, 221)
24	-3.1	-27.3	1	0.85	0.05	0.323	wf2	(326, 484)
25	-44.5	34.4	1	0.75	-0.01	0.216	wf3	(468, 398)
26	-2.1	21.6	1	0.82	0.03	0.140	wf3	(198, 49)
27	-2.7	-5.5	1	0.64	-0.01	0.287	wf2	(151, 354)
28	-29.5	38.7	3	0.12	0.06	0.915	wf3	(322, 346)
29	23.4	48.8	4	0.25	0.16	0.760	wf4	(132, 145)
30	-26.5	15.4	4	0.53	0.01	0.451	wf3	(433, 140)
31	-15.7	56.6	4	0.00	0.06	0.879	wf3	(104, 413)
32	8.3	-4.3	1	0.63	0.01	0.167	wf2	(205, 259)
33	-8.2	4.2	1	0.79	-0.04	0.194	wf2	(39, 342)
34	12.9	-1.8	4	0.01	0.15	0.654	wf2	(211, 207)
35	-3.2	3.0	1	0.33	0.02	0.146	wf2	(79, 308)
36	8.5	-1.6	2	0.00	0.06	0.353	wf2	(186, 242)
37	-39.9	37.4	4	0.38	0.11	1.317	wf3	(410, 395)
38	-24.6	38.7	1	0.28	0.02	0.118	wf3	(280, 319)
39	3.0	36.9	4	0.00	0.20	0.891	wf3	(69, 142)
40	34.3	43.5	1	0.44	-0.01	0.370	wf4	(25, 206)
41	4.6	52.8	4	0.00	0.14	0.551	wf4	(267, 21)
42	-2.8	52.7	3	0.04	0.12	0.471	wf3	(21, 306)
43	-38.2	12.2	3	0.55	0.10	0.441	wf3	(546, 179)
44	-7.3	-11.1	1	0.95	0.07	0.310	wf2	(169, 424)
45	-39.2	-6.2	4	0.71	0.02	0.282	wf3	(663, 37)
46	-41.1	14.0	4	0.01	0.07	0.581	wf3	(562, 211)
47	-27.1	19.5	1	0.01	0.01	0.234	wf3	(415, 178)
48	12.2	6.2	5	0.64	0.05	0.022	wf2	(141, 166)
49	1.1	8.8	4	0.70	0.07	0.472	wf2	(57, 238)
50	-6.0	-16.9	1	0.01	0.04	0.225	wf2	(225, 446)
51	8.8	-51.6	4	0.00	0.23	0.377	wf2	(595, 532)
52	-7.4	-21.5	1	0.54	0.10	0.145	wf2	(255, 488)
53	9.1	-14.0	0	0.59	0.03	0.235	wf2	(291, 304)
54	-23.3	25.8	3	0.00	0.32	0.506	wf3	(343, 209)
55	29.9	-10.4	5	0.83	0.07	0.137	wf2	(384, 118)
56	0.1	4.1	5	0.93	0.04	0.390	wf2	(88, 275)
57	-2.8	-54.9	4	0.00	0.06	0.583	wf2	(555, 648)
58	-18.0	-6.4	2	0.20	-0.11	0.506	wf2	(73, 484)
59	-53.6	13.9	4	0.17	-0.12	0.157	wf3	(658, 288)

^aClassification scheme from Stanford et al. (2002), 1 = E/S0, 2=Sa/Sb, 3=Sc/Sd, 4=Irr, 5=Merger and/or disturbed.

TABLE 11
3C210 HST NICMOS IMAGING DATA

ID	R.A. J2000	Dec. J2000	Class ^a	B/T	Res.	R _h (")	Pointing	Pos.
2	21.7	36.7	1	0.36	0.06	0.243	3	(186,106)
3	0.0	0.0	4	0.38	0.15	0.507	1	(135,70)
4	-6.5	27.8	4	0.73	0.66	0.262	3	(138,243)
8	-11.6	12.7	1	0.04	0.01	0.135	1	(51,79)
9	-21.4	7.3	1	0.49	0.13	0.187	1	(46,135)
10	21.8	54.8	2	0.33	0.07	0.331	3	(116,52)
11	-44.8	6.5	2	0.29	0.09	0.231	2	(238,227)
12	25.8	46.6	1	0.54	0.11	0.176	3	(161,60)
14	-16.5	15.8	2	0.68	0.03	0.074	1	(25,91)
17	-8.0	13.6	1	0.48	0.05	0.101	1	(59,63)
19	-37.5	14.3	4	0.41	0.10	0.234	2	(229,174)
21	-2.5	-6.7	2	0.91	0.04	0.205	1	(116,99)
22	-3.8	9.5	1	0.12	0.07	0.087	1	(86,58)
23	2.5	10.1	4	0.48	0.17	0.345	1	(102,32)
24	-3.1	-27.3	1	0.48	0.05	0.117	1	(236,160)
25	-44.5	34.4	1	0.82	0.15	0.061	2	(132,141)
26	-2.1	21.6	1	0.52	0.07	0.051	1	(43,17)
27	-2.7	-5.5	1	0.33	0.03	0.092	1	(150,96)
28	-29.5	38.7	3	0.21	0.05	0.332	2	(159,70)
29	23.4	48.8	4	0.21	0.06	0.341	3	(144,66)
32	8.3	-4.3	1	0.76	0.11	0.04	1	(176,49)
33	-8.2	4.2	1	0.64	0.06	0.059	1	(95,91)
34	12.9	-1.8	4	0.00	0.03	0.254	1	(179,24)
35	-3.2	3.0	1	0.97	0.05	0.051	1	(115,74)
36	8.5	-1.6	2	0.35	0.06	0.136	1	(167,41)
37	-39.9	37.4	4	0.23	0.13	0.56	2	(134,113)
38	-24.6	38.7	1	0.45	0.05	0.059	2	(173,50)
39	3.0	36.9	4	0.16	0.07	0.395	3	(132,179)
40	34.3	43.5	1	0.49	0.03	0.14	3	(197,38)
42	-2.8	52.7	3	0.41	0.07	0.223	3	(52,154)
43	-38.2	12.1	3	0.93	0.02	0.371	2	(237,183)
44	-7.3	-11.	1	0.49	0.05	0.064	1	(159,130)
45	-39.2	-6.2	4	0.97	0.03	0.083	1	(49,244)
47	-27.1	19.5	1	0.42	0.02	0.117	2	(240,119)
49	1.1	8.8	4	0.58	0.11	0.177	1	(104,39)
50	-6.0	-16.9	1	0.58	0.04	0.103	1	(187,141)
52	-7.4	-21.5	1	0.46	0.05	0.086	1	(201,161)
53	9.1	-14.0	0	0.79	0.02	0.072	1	(218,71)
56	0.1	4.1	5	0.57	0.03	0.086	1	(119,58)
59	-53.6	13.9	4	0.00	0.27	0.353	2	(183,238)

^aClassification scheme from Stanford et al. (2002), 1 = E/S0, 2=Sa/Sb, 3=Sc/Sd, 4=Irr, 5=Merger and/or disturbed.

TABLE 12
RDCS 0848+4453 HST WFPC2 IMAGING DATA

ID	δ_x (")	δ_y (")	Class ^a	B/T	Res.	R _h (")	Chip	Pos.
1	33.0	42.9	0	0.41	0.46	0.324	wf4	(319, 461)
2	-71.7	-2.4	0	0.00	-3.42	0.132	wf2	(24, 614)
3	-10.2	-30.0	2	0.65	0.02	0.599	wf2	(369, 250)
4	0	0	1	0.27	0.00	0.999	pc	(202, 169)
5	-30.9	-30.0	5	0.00	0.12	0.083	wf2	(346, 232)
6*	-37.5	-0.6	4	0.36	0.03	0.547	wf2	(43, 271)
6*	-37.5	-0.6	4	0.77	0.16	0.439	wf2	(44, 266)
6*	-37.5	-0.6	4	0.55	0.06	0.529	wf2	(40, 265)
7	-24.8	-49.8	2	0.01	0.11	1.573	wf2	(554, 197))
8	-51.0	25.8	2	0.52	0.01	0.464	wf3	(381, 221)
9	2.4	41.1	1	0.70	0.01	0.602	wf4	(326, 150)
10	41.4	37.8	0	0.00	0.25	0.787	wf4	(262, 542)
11	3.0	19.2	1	0.54	0.07	0.522	wf4	(108, 135)
12	-7.8	-6.6	2	0.41	0.06	0.683	pc	(13, 297)
13	-6.0	16.2	1	0.37	0.03	0.432	wf4	(86, 43)
14	-26.4	-5.4	4	0.08	0.10	1.047	wf2	(104, 162)
15	-31.5	10.8	2	0.23	0.04	0.217	wf3	(202, 49)
16	21.6	4.8	4	0.00	0.10	0.663	pc	(686, 107)
17	11.4	-2.1	1	0.34	-0.04	0.485	pc	(450, 242)
18	-25.5	-6.9	2	0.34	0.08	0.415	wf2	(118, 154)
19	-33.6	69.3	0	0.23	0.14	0.778	wf3	(161, 641)
20	21.6	26.1	3	0.01	0.03	0.909	wf4	(156, 332)
21	-32.7	21.6	1	0.14	0.05	0.589	wf3	(201, 159)
22	-20.1	-3.6	1	0.34	0.02	0.264	wf2	(91, 96)
23	9.0	25.5	1	0.95	0.02	0.327	wf4	(164, 204)
24	-50.7	31.5	5	0.02	0.04	0.033	wf3	(373, 278)
25	-41.1	60.6	0	0.00	0.75	0.251	wf3	(246, 560)
26	36.0	27.3	4	0.01	0.16	0.564	wf4	(157, 478)
27	-25.2	8.1	2	0.24	0.02	0.478	wf3	(141, 15)
28	-58.2	-37.8	0	0.00	0.19	0.949	wf2	(402, 513)
29	-45.9	-7.5	3	0.01	0.09	0.477	wf2	(99, 360)
30	-9.6	-51.9	2	0.00	0.15	0.579	wf2	(596, 40)
31	-54.9	-0.9	4	0.00	0.15	0.457	wf2	(25, 441)
32	-33.6	31.2	4	0.74	0.00	0.285	wf3	(202, 257)
33	-44.7	-65.4	0	0.17	0.00	0.461	wf2	(699, 406)
34	3.6	13.5	5	0.69	0.03	0.018	wf4	(47, 135)
35	-66.6	-45.0	0	0.32	-0.02	0.233	wf2	(464, 609)
36	-24.6	34.2	4	0.36	0.06	0.599	wf3	(109, 278)
37	-70.5	14.4	2	0.35	0.07	0.282	wf3	(591, 125)
38	-54.3	6.9	4	0.00	0.16	1.093	wf3	(435, 34)
39	-20.1	-7.5	2	0.41	0.06	0.683	pc	(13, 297)
40	10.8	20.1	1	0.35	-0.04	0.524	wf4	(108, 215)
41	-44.4	66.9	0	0.86	0.01	0.210	wf3	(274, 627)
42	3.6	3.9	1	0.03	-0.01	0.713	pc	(285, 91)
43	14.7	39.3	1	0.28	-0.02	0.261	wf4	(298, 274)
44	9.9	-12.3	1	0.01	0.01	0.716	pc	(393, 467)
45	-79.8	9.9	4	0.20	0.08	0.824	wf3	(692, 89)
46	-77.1	-27.6	0	0.00	0.26	0.273	wf2	(273, 699)
47	-54.9	-43.8	0	0.09	0.11	0.446	wf2	(458, 487)
48	-43.8	-3.3	4	0.01	0.20	0.368	wf2	(63, 335)
49	-79.8	18.0	0	0.01	0.16	0.671	wf3	(680, 172)
50	-0.9	12.9	2	0.01	0.06	0.329	wf4	(45, 91)
51	-21.6	48.6	0	0.04	0.21	0.747	wf3	(63, 420)
52	34.8	57.9	0	0.62	0.02	0.186	wf4	(467, 495)
53	1.8	-10.2	2	0.76	-0.01	0.399	pc	(217, 400)
54	-20.4	-33.0	5	0.42	0.02	0.097	wf2	(389, 132)
55	-39.9	-31.8	4	0.06	-0.09	0.649	wf2	(356, 323)
56	-19.5	1.5	3	0.04	0.08	0.390	wf2	(41, 84)
57	-7.2	-1.2	5	0.23	0.10	0.064	pc	(38, 180)
58	12.0	40.8	3	0.04	0.12	0.703	wf4	(317, 247)
59	-35.4	-61.8	0	0.01	0.03	0.236	wf2	(672, 310)
60	-65.4	-51.6	0	0.96	0.04	0.089	wf2	(529, 607)
61	-35.1	-57.9	0	0.46	0.08	0.306	wf2	(632, 301)
62	-1.2	-15.6	3	0.05	0.07	1.559	pc	(137, 512)
63	-31.8	-15.0	2	0.00	0.04	0.569	wf2	(191, 228)
64	-5.7	10.8	1	0.51	0.01	0.305	wf4	(29, 39)
65	17.7	47.1	2	0.01	0.13	0.196	wf4	(374, 310)
66	-22.2	27.3	4	0.01	0.22	0.610	wf3	(91, 207)
67	-44.4	26.4	1	0.59	0.00	0.118	wf3	(315, 219)
68	-66.6	-11.4	0	0.86	-0.05	0.323	wf2	(120, 571)
69	21.6	16.5	3	0.28	0.06	0.493	wf4	(59, 322)
70	-4.8	-4.2	4	0.01	0.19	0.949	pc	(89, 251)

^aClassification scheme from Stanford et al. (2002), 1 = E/S0, 2=Sa/Sb, 3=Sc/Sd, 4=Irr, 5=Merger and/or disturbed.

TABLE 13
RDCS 0848+4453 NICMOS CAMERA 3 IMAGING DATA

ID	δ_x (")	δ_y (")	Class ^a	B/T	Res.	R_h (")	Pointing	Pos.
3	-10.2	-30.0	2	0.49	0.05	0.207	3	(141,124)
4	0	0	1	0.59	0.06	0.437	2	(147,226)
5	-30.9	-30.0	5	0.00	0.10	0.031	3	(63,190)
6	-37.5	-0.6	4	0.00	0.37	0.298	1	(197,164)
8	-51.0	25.8	2	0.54	0.05	0.159	1	(61,108)
9	2.4	41.1	1	0.44	0.15	0.276	2	(23,65)
11	3.0	19.2	1	0.60	0.04	0.259	2	(96,145)
12	-7.8	-6.6	2	0.65	0.06	0.170	3	(75,27)
13	-6.0	16.2	1	0.71	0.08	0.241	2	(72,185)
15	-31.5	10.8	2	1.00	0.08	0.073	1	(183,102)
16	21.6	4.8	4	0.54	0.24	0.506	2	(213,139)
17	11.4	-2.1	1	0.62	0.04	0.108	2	(197,198)
20	21.6	26.1	3	0.00	0.11	0.401	2	(144,59)
21	-32.7	21.6	1	0.12	0.07	0.292	1	(143,65)
22	-20.1	-3.6	1	0.27	0.04	0.121	3	(19,55)
23	9.0	25.5	1	0.72	0.06	0.139	2	(99,102)
24	-50.7	31.5	5	0.39	0.13	0.001	1	(44,86)
27	-25.2	8.1	2	0.73	0.13	0.325	1	(214,92)
29	-45.9	-7.5	3	0.03	0.18	0.359	1	(187,217)
30	-9.6	-51.9	2	0.00	0.06	0.242	3	(215,206)
31	-54.9	-0.9	4	0.17	0.11	0.198	1	(133,221)
32	-33.6	31.2	4	0.56	0.04	0.095	1	(109,32)
34	3.6	13.5	5	0.06	0.14	0.020	2	(117,165)
37	-70.5	14.4	2	0.48	0.06	0.127	1	(25,215)
38	-54.3	6.9	4	0.46	0.19	0.658	1	(110,190)
39	-20.1	-7.5	2	0.82	0.06	0.110	3	(30,69)
40	10.8	20.1	1	0.58	0.02	0.199	2	(122,117)
42	3.6	3.9	1	0.42	0.06	0.192	2	(147,200)
43	14.7	39.3	1	0.44	0.06	0.115	2	(76,31)
44	9.9	-12.3	1	0.93	0.18	0.235	2	(225,242)
48	-43.8	-3.3	4	0.00	0.16	0.236	1	(182,195)
50	-0.9	12.9	2	0.00	0.16	0.148	2	(102,181)
54	-20.4	-33.0	5	0.95	0.02	0.023	3	(112,169)
55	-39.9	-31.8	4	0.00	0.10	0.465	3	(34,226)
58	12.0	40.8	3	0.10	0.05	0.295	2	(60,34)
62	-1.2	-15.6	3	0.44	0.04	0.304	3	(128,40)
64	-5.7	10.8	1	0.48	0.04	0.134	2	(91,205)
67	-44.4	26.4	1	0.69	0.02	0.035	1	(84,85)
69	21.6	16.5	3	0.00	0.28	0.198	2	(176,95)

^aClassification scheme from Stanford et al. (2002), 1 = E/S0, 2=Sa/Sb, 3=Sc/Sd, 4=Irr, 5=Merger and/or disturbed.

This figure "holden.fig1.jpg" is available in "jpg" format from:

<http://arxiv.org/ps/astro-ph/0503367v2>

This figure "holden.fig2.jpg" is available in "jpg" format from:

<http://arxiv.org/ps/astro-ph/0503367v2>

This figure "holden.fig3.jpg" is available in "jpg" format from:

<http://arxiv.org/ps/astro-ph/0503367v2>

This figure "holden.fig4.jpg" is available in "jpg" format from:

<http://arxiv.org/ps/astro-ph/0503367v2>

This figure "holden.fig5.jpg" is available in "jpg" format from:

<http://arxiv.org/ps/astro-ph/0503367v2>

This figure "holden.fig6.jpg" is available in "jpg" format from:

<http://arxiv.org/ps/astro-ph/0503367v2>

This figure "holden.fig7.jpg" is available in "jpg" format from:

<http://arxiv.org/ps/astro-ph/0503367v2>

This figure "holden.fig8.jpg" is available in "jpg" format from:

<http://arxiv.org/ps/astro-ph/0503367v2>

This figure "holden.fig9.jpg" is available in "jpg" format from:

<http://arxiv.org/ps/astro-ph/0503367v2>

This figure "holden.fig10.jpg" is available in "jpg" format from:

<http://arxiv.org/ps/astro-ph/0503367v2>